2018

Thermal transport and thermal structural domain in microfibers

Bowen Zhu
Iowa State University

Thermal transport and thermal structural domain in microfibers

by

Bowen Zhu

A dissertation submitted to the graduate faculty

in partial fulfillment of the requirement for the degree of

DOCTOR OF PHILOSOPHY

Major: Mechanical Engineering

Program of Study Committee
Xinwei Wang, Major Professor
Xianglan Bai
Nastaran Hashemi
Guowen Song
Yue Wu

The student author, whose presentation of the scholarship herein was approved by the program of study committee, is solely responsible for the content of this dissertation. The Graduate College will ensure this dissertation is globally accessible and will not permit alterations after a degree is conferred.

Iowa State University

Ames, Iowa

2018

TABLE OF CONTENTS

ACKNOWLEDGEMENT

I would like to thank my committee chair, Xinwei Wang, and my committee members, Xianglan Bai, Nastaran Hashemi, Guowen Song, Yue Wu for their guidance and support throughout this research.

I would also like to thank my family, friends, colleagues, and the department staff for making my time at Iowa State University a wonderful experience.

The support to this research from National Science Foundation (CBET1235852, CMMI1264399), Department of Energy (DENE0000671, DE-EE0007686), and Iowa Energy Center (MG-16-025, OG-17-005) is gratefully acknowledged.

ABSTRACT

Microfibers have been playing a fundamental role in heat dissipation in composite structures like fiber-reinforced polymer and ceramic matrix composite. The growth of industrial application calls out a demand for experimental investigation on thermal properties and structure of microfibers for continued improvement on performance.

This work furthers the current understanding of structure-property relationship in microfibers through use of combined thermal characterization and structure characterization on the same samples. Human hair, ultra-high molecular weight polyethylene (UHMW-PE) microfiber and silicon carbide (SiC) microwire are sampled as representatives of natural polymer fiber, synthetic polymer fiber and ceramic fiber, respectively. Thermal characterization for them was carried out in the temperature range between 20 K and room temperature using the transient electrothermal (TET) technique. Structure analysis includes x-ray diffraction (XRD) analysis and Raman spectroscopy.

The investigation on human hair finds that the short range order in protein (1-2 nm in size) can be revealed by the phonon life time at low temperatures. The grain boundary-induced phonon mean free path, named as structural thermal domain (STD) size in this work, is found comparable with the crystallite size given by XRD and the rigid domain size given by nuclear magnetic resonance. The structure difference between grey hair and black hair is also revealed by the difference in STD size.

In the study on UHMW-PE microfibers, a metal-like thermal conductivity (51 W/m·K) is achieved by heat stretching a highly crystalline (92%) and oriented sample, Spectra S-900. The STD size is enlarged by more than three times by the stretching process. However, XRD pole

figure analysis presents negligible change in crystallite size and crystallite orientation and even shows an unexpected decrease in crystallinity from 92% to 83%. Polarized Raman spectroscopy suggests improved alignment of amorphous chains. Those evidence that the improvement in thermal conductivity should be enabled by the restructuring of amorphous phase.

The investigation on SiC microwires is a comparative study for three advanced 3C-SiC microwires, including Sylramic, Hi-Nicalon S and a sample fabricated by laser chemical vapor deposition (LCVD). The temperature dependence of thermal properties of the three samples is given in this work. Unlike the hair keratin and the UHMW-PE that contain molecular chains, 3C-SiC possess compact and cross-linked molecular structure. Probably due to this, the STD size is found one order of magnification smaller than, instead of being close to, the crystalline size.

CHAPTER 1. INTRODUCTION

1.1 Thermal Characterization of Microfibers

The growing application of microfibers requires further understanding of their thermal properties. In contrast to the extensive studies on the thermal properties of bulk materials, the experimental measurements on microfibers are relatively few. The challenge for thermal characterization of microfibers is mainly due to the large surface-to-volume ratio, which creates significant radiation heat loss. Conventional steady-state methods are prone to the error induced by radiation heat loss.[1, 2] During the past two decades, transient methods, including time-domain thermoreflectance (TDTR), 3-omega[3-5] and transient electro-thermal (TET) technique,[6] have been developed to overcome the challenges. Those methods successfully reduce the radiation effect by extracting thermal properties from a transient thermal transport process within a short period of time. TDTR is a laser-based technique that introduces fast laser heating using a pump laser and detects the temperature change using a probe laser. It allows the measurement of thermal properties with a spatial resolution because heating and probing can be localized in microscale. TDTR is designed for measurement of bulk or film structure. To measure a microfiber, a smooth cross section should be created, which can be challenging.[7] TET and 3 omega are both electrothermal techniques. 3-omega can measure the three thermal properties (thermal conductivity, thermal diffusivity and heat capacity) at the same time, but it demands that a sample should have a linear electrical resistance-temperature (*R*-*T*) correlation within the temperature range of measurement. Therefore, 3-omega method is not suitable for semi-conductive materials. TET method has the advantage of a shorter measurement time and simplicity of signal processing. However, TET can only measure thermal diffusivity without the knowledge of *R*-*T* correlation.

1.2 Structure-property Correlation: Thermal Reffusivity and Structural Thermal Domain

In recent five years, a new concept: thermal reffusivity has been introduced to explain the correlation between thermal properties and domain structure in materials.[8-10] The thermal properties of solids depend on the behavior of heat carriers in micro/nano scale. In non-conductive solids, phonon is the heat carrier. Kenetic theory of gases with relaxation time approximation bridges the thermal conductivity and phonon propagation in the expression as: $k = \rho c_p v l / 3,$ where ρc_p, v and l are volumetric heat capacity, phonon group velocity and phonon mean free path (MFP), respectively. The phonon MFP is effected by the scattering process between phonons themselves l_p and between phonons and defects. Considering the dominating role of grain boundaries l_b for the samples studied in this work, we disregard other types of defects (i.e. impurties and point defects) in the modeling. The contribution from both scattering effects can be described by Matthiessen's rule: $l^{-1} = l_p^{-1} + l_b^{-1}$. At low temperature, the phonon-phonon scattering term l_p^{-1} can be considered to be proportional to the phonon population because two-body interaction has an overwhelmingly high possibility at low temperature. Therefore, $l_p^{-1} = A_0 e^{-T_D/2T}$, where A_0 is a constant and $e^{-T_D/2T}$ is the Boltzmann factor that compares the phonon population at T and at T_D, the Debye temperature.[11] T_D is an intrinsic property determined by crystal structure. The thermal conductivity is then expressed as

$$k = \frac{1}{3}\rho c_p v (l_b^{-1} + A_0 l_b e^{-T_D/2T})^{-1} \quad (1)$$

Thermal reffusivity Θ, reciprocal of thermal diffusivity, is introduced for a more chubprecise and physically meaningful expression, considering both k and ρc_p are temperature dependent and v is not sensitivity to temperature change. By subtituting Θ, eqn. 1 is written as

$$\Theta = \frac{\rho c_p}{k} = \frac{3}{vl} = \frac{3}{v}\left(\frac{1}{l_b} + A_0 e^{-T_D/2T}\right) \quad (2)$$

Equation 2 suggests a temperature dependence of Θ: As temperature goes down to 0 K limit, Θ decreases with a decreasing speed until arrive at an intercept Θ_0 at 0 K. The structural domain (STD) size is defined as defect-induced phonon mean free path at 0 K and can be described by the thermal reffusivity model as $l_b = 3/v\Theta_0$. Similar to other particle scattering effect (e.g. x-ray photon) induced by material structure, phonon scattering is also determined by material structure. Therefore, a connection between thermal property (Θ) and material structure is established.

Recent experiments have shown that thermal reffusvity theory fits well with experimental observation on deoxyribonucleic acid (DNA) fiber and graphene-based materials.[8] [9, 10] In DNA fibers, STD is found to be twice of the length of a DNA helix.[8] In the investigation on graphene foam, graphene foam is found to have smaller STD and similar T_D compared with pyrolytic graphite, consistent with the fact that graphene foam is more defective but similar in crystalline arrangement.[9] For highly diffective system like graphene aerogel, Θ is found independent of temperature, suggesting the dominance of phonon-defect scattering.[10]

1.3 Research Progress on High-thermal-conductivity Polymers

High-thermal-conductivity polymers are very sought-after for application in flexible electronics thermal design as the substrate for excellent heat dissipation, apparel of reduced heat stress to quickly re-spread the accumulated heat from sensitive body areas and to conduct the heat to environment, and as fillers to make high-performance material interfaces used in CPU cooling. The demand comes from their existing features including light weight, low cost and extraordinary mechanical properties.[12-14] However, *k* of common synthetic polymers, including polyethylene terephthalate (PET), low density polyethylene (LD-PE), polypropylene

(PP) and poly (methyl methacrylate) (PMMA), falls in the range of 0.1-0.3 W/m·K.[15-17] Attempts have been made to enhance *k* of polymers. Crystallinity and molecular orientation are two key factors that influence *k*. The high *k* that comes from high crystallinity is due to the higher *k* of a crystalline polymer than its amorphous counterpart. For example, at room temperature (RT) PE of 81% crystallinity has 70% higher *k* than PE of 43% crystallinity.[16] Besides, *k* enhancement can also be driven by molecular alignment,[18-22] with the understanding that the covalent bonds along polymer chains should sustain better energy transport than the van de Waals interaction between neighboring chains.[23] In practice, mechanical stretching is an effective way to enhance *k* when both chain alignment and increased crystallinity can be observed. For instance, *k* of polyacetylene film up over 10 W/m·K with approximate 500% elongation by Piraux *et al*.[20] *k* and degree of orientation are found increased for PE molecules in the molecular dynamic simulation by Liu *et al.*[24] The coincidence of chain alignment and anisotropic *k* is observed experimentally for amorphous polymers including PMMA and polycarbonate by Kurabayashi.[22]

The heat stretching process of PE for the production of highly thermal conductive fibers has been the subject of extensive research for several decades. High *k* has been achieved in laboratory (9-104 W/m·K)[7, 21, 25-27] and predicted by numerical simulation for a single PE chain (~350 W/m·K).[28] The highest *k* for PE film is 41 W/m·K, achieved by ultra-drawing UHMW-PE single crystal mat produced by Kanamoto's method to a strain ratio of 350 with a strain rate of 0.083 s^{-1} at 125 °C in the work by Choy *et al*.[21, 29] The thermal characterization employs laser-flash technique[30] at 160-300 K and steady heat flow method below 160 K. *k* of UHMW-PE microfibers are measured to be ~60 W/m·K (DSM Dyneema) using steady heat flow method, 12-17 W/m·K (DSM Dyneema and Honeywell Spectra) using time-domain

thermoreflectance (TDTR) and 20-23 W/m·K (Honeywell Spectra) by TET.[7, 25, 31] *k* values in ref. [21] and [25] could be overestimated because steady-state method is employed without subtracting the radiation effect, which is not negligible for a sample of large surface-to-volume ratio. *k* of electrospun PE nanofibers is measured to be 9.3 W/m·K by Ma *et al.*[26] using microfabricated thermal device.[32] Recently, *k* of PE nanofiber has been claimed to reach an astonishing value as high as 104 W/m·K by ultra-drawing in the work by Shen *et al.*[27] The optimum sample is elongated to 131 nm in diameter and 290 μm in length by an estimated draw ratio of 60-800. Thermal characterization is based on a steady-state method using a bi-material cantilever as temperature sensor.

1.4 Scope of Present Work

In this work, the experimental detail about the TET technique for thermal characterization is introduced in chapter 2, including the experimental setup, physics model and error analysis. In chapter 3, the thermal reffusivity of human hair (black and grey) is investigated from RT to 20 K. A comparison is made between the domain sizes determined by phonon scattering, x-ray scattering and nuclear magnetic resonance. In chapter 4 and 5, the research on UHMW-PE microfiber is presented. The process to optimize the stretching condition for high thermal conductivity is presented in chapter 4. The discussion on the reason for the improvement of thermal conductivity is in chapter 5. Low-temperature thermal characterization is performed for structural thermal domain analysis. Structural analysis techniques, including XRD pole figure and polarized Raman spectroscopy, are used to investigate crystallinity, crystallite size and orientation, and chain alignment before and after stretching. Thermal characterization of three advanced silicon carbide microwires is presented in chapter 6.

CHAPTER 2. TRANSIENT ELECTRTHERMAL TECHNIQUE

This chapter introduces a technique for measuring the thermal properties of microfibers. The technique, transient electrothermal technique (TET), uses square current to introduce Joule heating effect in a short period of time.

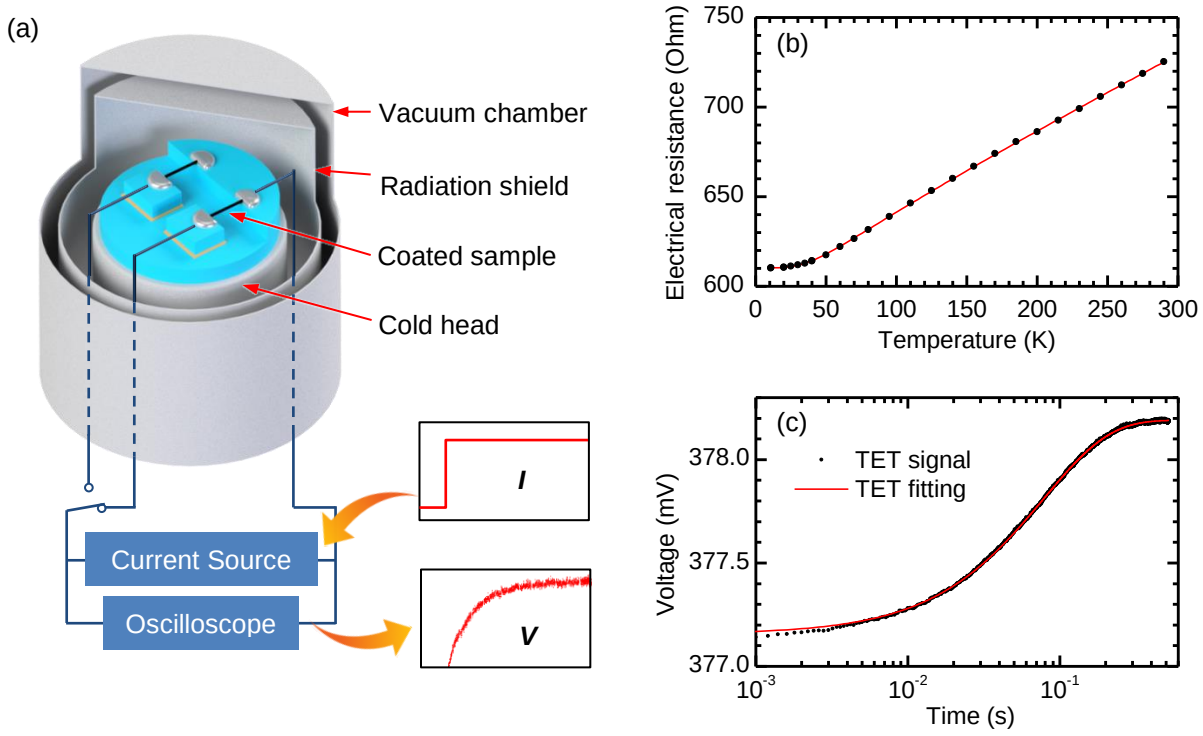

Figure 2.1 Configuration and data processing of TET experiment. (a) Set-up of a cryogenic TET system. In a vacuum chamber (0.4-0.7 mTorr) with radiation shield, two microwire samples are suspended between aluminum electrodes. Both ends of a sample are covered by silver paste. The electrodes are electrically insulated from each other by thin mica layers and connected by ceramic screws. The current source provides a step current input. The oscilloscope monitors the voltage response in time domain. The aluminum electrodes are placed on the cold head of cryostat. (b) Temperature dependence of electrical resistance of the 20-nm iridium coating on the LCVD-FFF sample (a silicon carbide sample to be discussed in Chapter 6). The black dots are the measured data and the red line is the fitting curve of Bloch-Grüneisen formula. (c) TET voltage signal in logarithmic time domain. The voltage signal is a response to a 0.52-mA step current input during measurement of the LCVD-FFF sample (1495 μm long and 34.3 μm thick) at 290 K.

The temperature change of a fiber sample is probed by electrical resistance of the metallic coating that has been deposited on the sample. The measured thermal properties include thermal diffusivity, thermal conductivity and volumetric heat capacity. By integrating with a cryogenic system, those thermal properties can be measured in the temperature range from RT to 20 K.

2.1 Setup

The experimental set-up of TET technique is presented in Figure 2.1a. The to-be-measured sample is suspended between two aluminum (Al) electrodes. Silver paste is employed to guarantee a sound electrical and thermal contact between Al electrode and sample fiber. The electrodes are connected to one another via alumina screws and thin mica layers. The sample holder composed of three aluminum electrodes is attached to a cold head with thermal grease. The temperature of the cold head is controlled by a monitoring/control unit (Lakeshore 335). Radiation heat loss is suppressed by shielding and convection by operating in a vacuum and reducing sample length (1-1.5 mm). To feed current input and record voltage output, a current source (Keithley 6221) and an oscilloscope (Tektronix DPO3052 or MDO3052) are parallel connected to the Al electrodes.

2.2 Process

The measurement generally proceeds by applying a step current through a metallic coating that has been deposited on an electrically insulating sample. Thermal properties can be extracted from the thermal response induced by Joule heating. The metallic coating also serve as temperature sensor since its electrical resistance is temperature dependent. For the samples measured in this work, 20-nm thick Ir layer (Quorum 150T S) has been sputter coated on the

sample fiber. The electrical resistance (R) of Ir coating is sensitive to temperature change between 20 and 300 K and follows Bloch-Grüneisen formula, as seen in Fig. 2.1b.[33] Therefore, the temperature rise will appear as a voltage rise on the screen of oscilloscope. An example of voltage evolution in response to a step current input is shown in Fig. 2.1c.

2.3 Physic Model

The heat transfer equation of the system can be simplified as a one-dimensional case. The governing equation regardless of thermal radiation is written as

$$\frac{\rho c_p \partial T}{\partial t} = k \frac{\partial^2 T}{\partial x^2} + \dot{q} \tag{3}$$

where $\dot{q}$ is the electrical heating power per unit volume of the sample. The initial condition of the problem is $T(x, t=0) = T_0$, where T_0 is the initial temperature of the sample. The boundary condition is $T(x=0, t) = T(x=L, t) = T_0$ due to the bulk electrodes being as heat reservoirs. By assuming a linear R-T correlation (dR/dT is actually nearly constant as seen in Fig. 2.1b within the limited temperature rise (ΔT, usually 1-5 K) of each measurement, Eqn. 3 can be solved analytically and the normalized voltage rise[$V^*(t)=(V(t)-V_0)/(V_\infty-V_0)$] mimics the normalized temperature[$T^*(t)=(T(t)-T_0)/(T_\infty-T_0)$], where V_0 is the initial voltage, V_∞ and T_∞ are the voltage and temperature at steady state, respectively. The solution can be written as:

$$V^*(t) = T^*(t) = \frac{96}{\pi} \sum_{m=1}^{\infty} \frac{1 - \exp[-(2m-1)^2 \pi^2 \alpha_{\text{eff}} t / L^2]}{(2m-1)^4} \tag{4}$$

where α_{eff} is effective value that contains the radiation and coating effect. By fitting $V^*(t)$, α_{eff}, the only unknown parameter in Eqn. 4 is obtained. The intrinsic α is obtained by subtracting the contribution of radiation and the Ir coating, which has been detailed elsewhere.[34] Here, we provide the expression of the solution:

$$\alpha = \alpha_{eff} - \frac{16\varepsilon\sigma T^3 L^2}{\pi^2 D\rho c_p} - \frac{L_{Lorenz} TL}{RA\rho c_p} \quad (5)$$

where ε is the surface emissivity, σ is Stefan-Boltzmann constant, L_{Lorenz} is the Lorenz number of the Ir coating, ε, ρc_p, D and A are the emissivity, diameter, volumetric heat capacity, and cross-sectional area of the fiber sample, respectively. For a more complete description of physical principle and experimental design about the TET technique, readers can be referred to literature.[6, 8, 31, 35]

CHAPTER 3. STRUCTURAL THERMAL DOMAIN IN HUMAN HAIR

This chapter reports the temperature-depedent behavior of thermal reffusivity of human hair (black and grey) in the temperature range between 20 K and RT. Sound agreement is found between the STD size and and the crystallite size meassured by XRD.

3.1 Sample Preparation

A grey hair sample and a black hair sample were collected from an individual hair strand from a 27-year-old Chinese female. The hair strand is grey at the tip (~8 cm long) and black near the end (~15 cm). 1-cm cut was collected from the center of each side. No chemical process was involved. The SEM images and the diameter measurement are presented in Fig.3.1a-b. The contribution of radiation and Iridium coating to heat transport is evaluated to be less than 8% over the total thermal diffusivity and has been subtracted in the result.

3.2 Result and Discussion

The Θ–*T* result is shown in Figure 3.1c. Θ of grey hair is lower than that of black hair by 42-47% throughout the entire temperature range. This indicates a reduced level of phonon-phonon scattering in grey hair. The thermal diffusivity of the white hair is higher than that of the black hair. This is probably due to the impaired inner structure. The Θ-*T* of hair samples exhibits a common trend: Θ decreases linearly with decreasing *T* as $T > 50$ K; below 50 K, Θ tends to be stable, leaving a residual value at 0 K. This behavior is different from the pattern of most of the crystallite materials and cannot be fitted using the thermal reffusivity model in equation (9). This linear Θ –*T* result is similar to that of carbon nanocoils material with polycrystalline-amorphous structure.[36] In their work, they attributed the linear behavior to the combined scattering effect

from both sp^2 graphite grain and sp^3 matrix. We speculate it to be a common behavior of materials with amorphous structures, but the coherent physical model for the linear Θ –T curves is not clear.

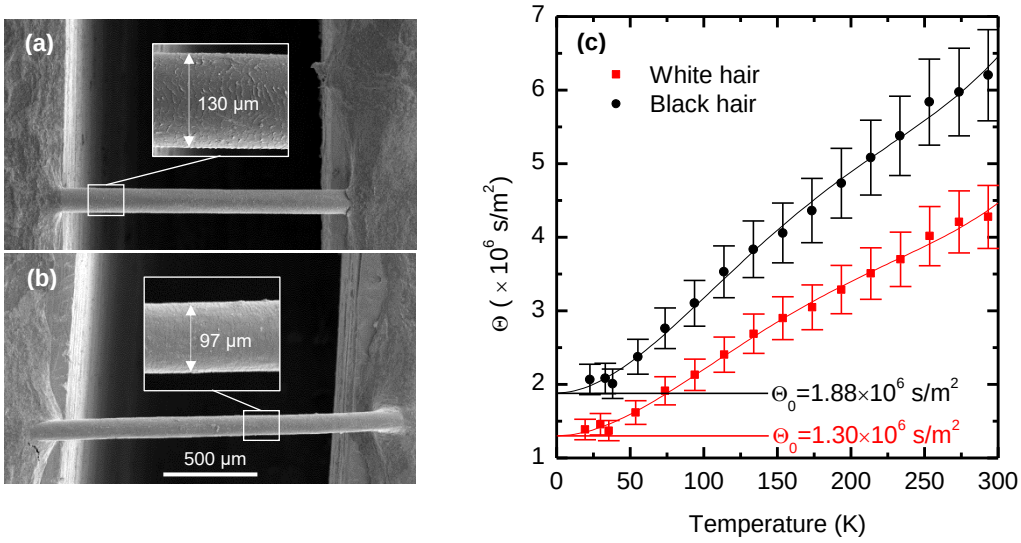

Figure 3.1 SEM images of (a) the black hair sample and (b) the grey hair sample. The samples are already coated with Iridium and suspended between electrodes for measurement. Insets of (a) and (b): Zoomed-in view for diameter measurement. (c) Thermal reffusivity as a function of temperature for both samples, with denoted residual thermal reffusivity. The lines are quadratic fitting curves, whose slope is fixed to zero at 0 K.

Although the Θ–T result cannot be fitted using the thermal reffusivity model, the residual thermal reffusivity at 0 K limit still provides information on the defect levels and STD sizes. By using a quadratic fitting curve to smooth the data and fixing the slope at 0 K to be zero, the value of Θ_0 is determined to be 1.30×10^6 S/ m^2 and 1.88×10^6 S/ m^2 for the grey hair and black hair respectively. With an average phonon velocity in hair samples (1000 m/s), the domain size is estimated as 1.6 nm for black hair and 2.31 nm for grey hair. Note that the average phonon velocity in hair is unknown so far, therefore the value used here is gauged from the determined values of other proteins.[37] Considering the phonon velocity in proteins is generally very low

and within the same order of magnitude, the error from the phonon velocity is expected to be small. Larger STD size in the grey hair sample illustrates that the grey hair contains less defect from the perspective of heat transport. This suggests that the grey hair experience a change which results in an increased domain size.

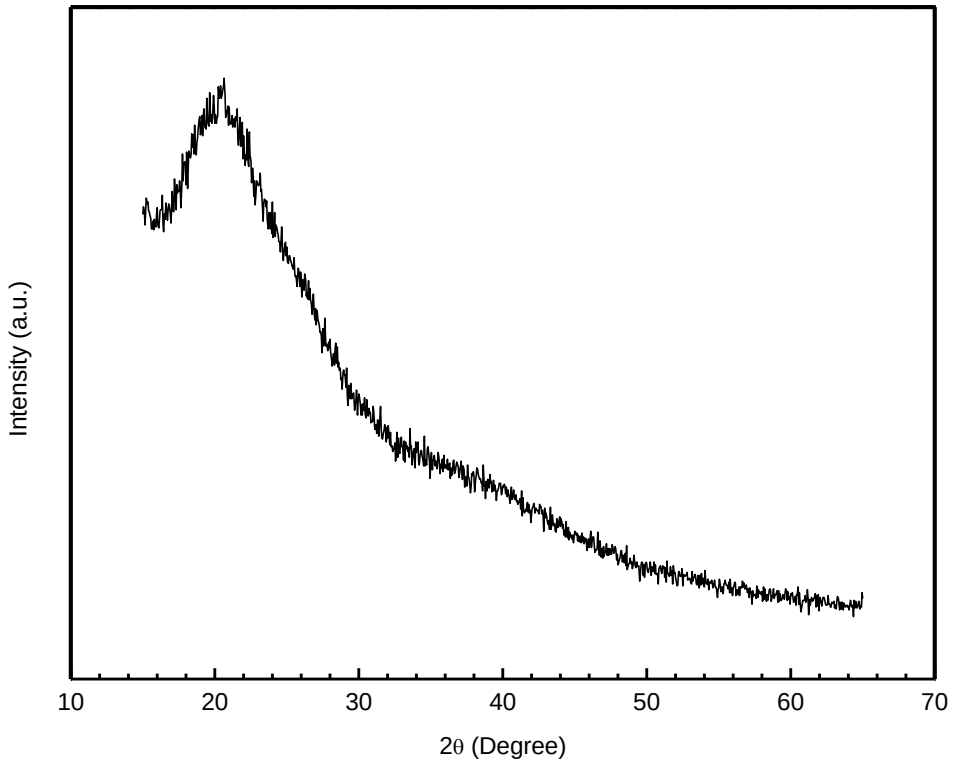

Figure 3.2 XRD pattern for human black hair. ~30 hair strands are aligned as a thin film for XRD characterization. The crystallite size extracted from the pattern is 1.8 nm.

XRD is also used to characterize the crystalline structure of black hair. The XRD pattern is shown in Fig. 3.2. By fitting the broad peak that may arise from the ordered structure of keratin, the average crystallite size in the black hair sample is determined as 1.8 nm for the, close to the STD size (1.6 nm) deduced from thermal analysis. This result demonstrates that the thermal reffusivity theory does give a comparable evaluation on the domain size of human hair. It should be noted that for the human hair sample, XRD peaks are not too broad to overshadow

the crystallite size information. However, it represents a limit for the XRD study on amorphous materials. For other amorphous materials, such as silkworm silk, the XRD peaks are almost invisible. This makes the domain size characterization using XRD becomes impossible for lots of amorphous materials. In addition, the STD size in human hair is also found comparable with the rigid domain size detected by nuclear magnetic resonance (NMR).[38] For the studied virgin hair (Caucasian human), bleached hair, and perm-waved hair sample, the particle sizes in rigid phase were measured to be 4.5, 5.5 and 3.0 nm by ^{1}H NMR analysis, respectively. For comparison, the STD values were measured to be 1.22, 1.97 and 1.75 nm, respectively. In spite of the difference in physical interpretation, the closeness of domain size values from both techniques postulated 1-5 nm grain structures in human hair.

CHAPTER 4. IMPROVEMENT OF THERMAL CONDUCTIVITY OF POLYETHYLENE

Till now, no other studies have reported high thermal conductivity comparable to the work by Choy *et al.* (41 W/m·K for single crystal mat) and Shen *et al* (104 W/m·K for nanofiber).[21, 27] In this chapter, we will introduce a heat stretching process that finally enhances the thermal conductivity of UHMW-PE microfiber to a metal-like level (51 W/m·K). This is the highest thermal conductivity for synthetic polymer microfiber, a form that can be applied in industrial level. Stretching conditions, including temperature and speed, and resultant thermal conductivity will be presented. The reason for the improvement will be discussed in Chapter 5.

4.1 Sample Preparation

Honeywell Spectra S-900, a commercial UHMW-PE fiber of high tensile modulus (73 GPa) and high crystallinity (92%), was supplied by Minifibers, Inc. in the form of 50 mm cut. Sample thickness varies between 40 and 55 μm. The density is 0.97 g/cm^3. Each sample fiber is further cut into two parts: 40 mm, for heat stretching, and 10 mm, as reference.

Heat stretching is performed by applying constant temperature and constant stretching speed to a sample fiber, followed by immediate cooling in air. The design of the heat stretching system is based on the fiber tapering method of Rudy and colleagues.[39] The setup of the system is presented in Figure 4.1. The stretching speed is controlled by two motorized translation stages (Thorlabs MTS50-Z8 and Z812B). The motion of the stages is delivered to the fiber via fishing lines (UHMW-PE multiple filaments), with flattened brass tubes and screws as connecter.

4.2 Heat Stretching

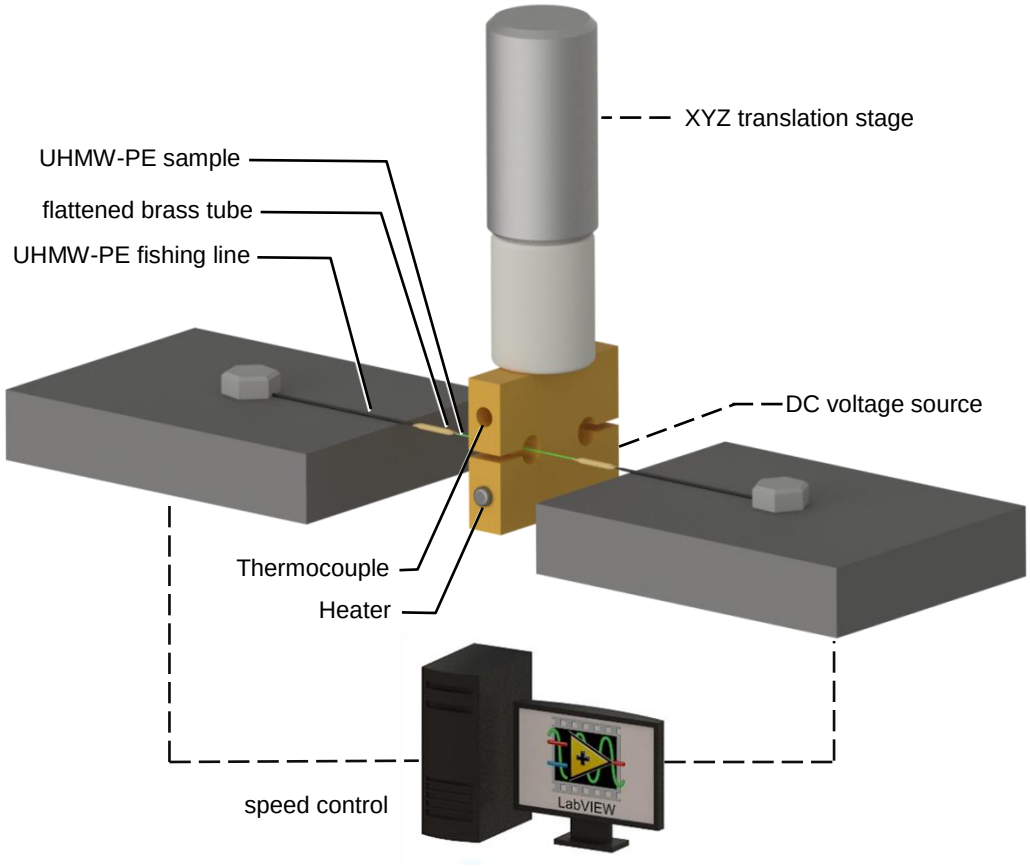

Figure 4.1 Setup of heat stretching system. An Al block is integrated with a cartridge heater and a thermocouple sensor to provide a constant temperature during stretching. The temperature gradient along sample fiber is estimated to be 10 ~ 40 K/mm, depending on center temperature. The center temperature of sample fiber is measured by calibrating it to the sensor temperature.

Temperature control is enabled by a thermocouple and a cartridge heater in an Al block. The fiber temperature has been calibrated to the temperature of the thermocouple in Al block. The elongation of fishing line has been verified to be negligible compared with that of the fiber. The to-be-stretched fiber is 35 mm long. The width of the Al block as heater is ~5 mm.

Based on the setup, heat stretching is performed as described: 1) The Al block is heated up to expected temperature and maintained stable ($\pm$1 ºC). 2) The to-be-stretched fiber is moved

into the fiber hole through the slit. 3) The two translation stages then move with a constant speed in opposite direction, until the sample reaches its expected maximum elongation (slightly smaller than the elongation at break for numerous samples). 4) The fiber is removed from the Al block once the elongation ends. The fiber is still suspended during cooling in air.

4.3 Effect of Heating Level and Stretching Speed

In this section, thermal conductivity of S-900 fibers before and after stretching is evaluated at room temperature. The effect of heat stretching condition on thermal conductivity will be presented. Thermal diffusivity is directly measured, instead of thermal conductivity. The volumetric heat capacity of S-900 is calculated by an interpolation between that of crystal PE and that of PE melt, which is considered completely amorphous.[31, 40, 41] The crystallinity for interpolation comes from XRD analysis. Thermal conductivity is obtained by $k = \alpha\rho c_{\mathrm{p}}$. In the error analysis, the error of thermal conductivity is the combined error from thermal diffusivity and heat capacity. However, the error of heat capacity is not considered here due to the difficulty of evaluation—Error analysis is not given in the referred literature. The ρc_p used in this work is nevertheless reliable because 1) the ρc_p of crystal PE is well-defined by both simulation and experiment,[40, 41] 2) the sample used in this work is highly crystalline (83-92%), and 3) for amorphous PE and crystal PE the difference in ρc_p is not significant (within 20% in the temperature range of 30-300 K).[41]

Heat stretching covers a temperature range of 116-135 ºC. The reason is that we cannot find significant elongation and k enhancement below 116 ºC. Initially, heat stretching has been performed between RT and 90 ºC in water bath. Low-temperature stretching leads to k enhancement of less than 4 W/m·K while k of original fibers can vary between 19 and 22 W/m·K.

Above 135 ºC, a fiber breaks nearly without resistance to applied force. It seems the majority of fiber content has molten, although the suspended fiber nevertheless holds its shape before stretching, possibly due to the very long molecular chain. The stretching speed includes three values for comparison: 6, 10 and 20 μm/s. Stretching at a speed over 20 μm/s limits the elongation and resultant *k* enhancement. 6 μm/s is the minimum speed given by the motorized translation stages. Therefore, the stretching conditions that are selected to present include 116-135 ºC as temperature range and 6-20 μm/s as speed range. Under such conditions, the strain rate is estimated to be between 0.008 s^{-1} and 0.016 s^{-1} by measuring local fiber width.

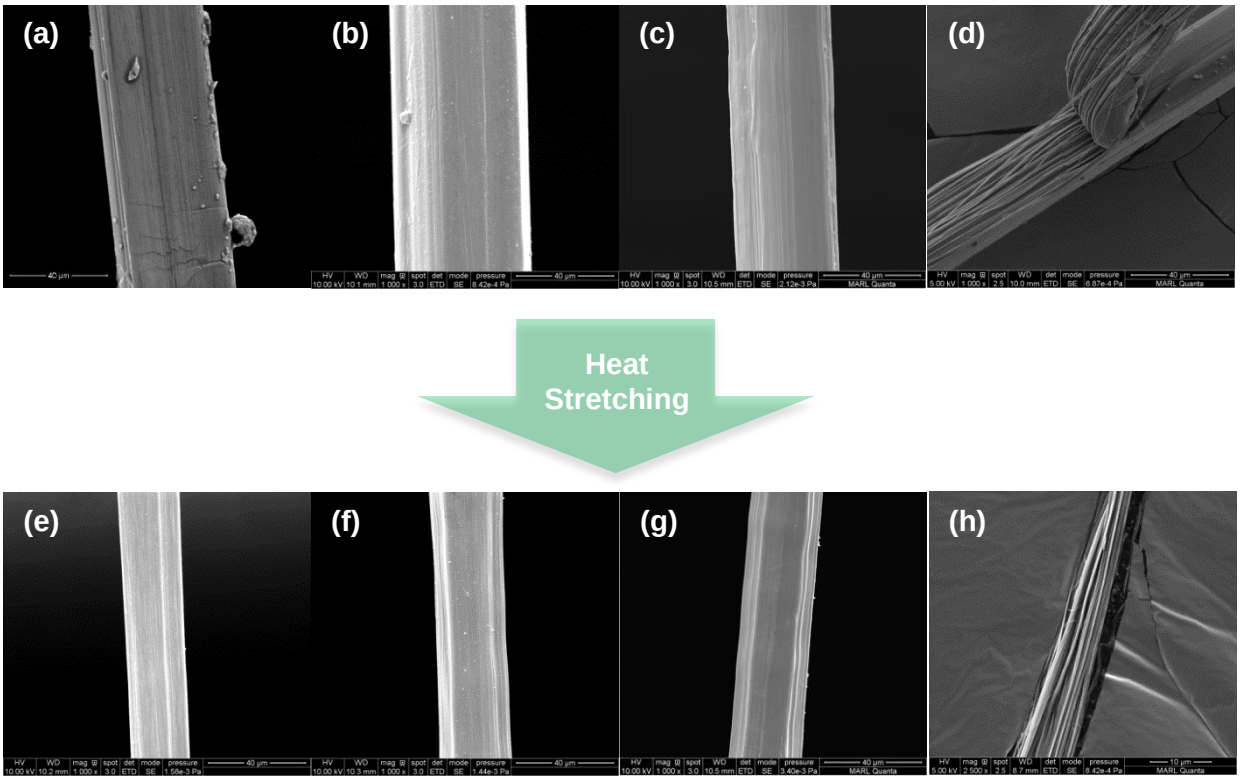

Figure 4.2 SEM images of UHMW-PE fibers before and after heat stretching. Sample A, B and C were stretched under three different condictions, as summarized in Table 4.1. (a-c) sample A-C before stretching: (e-f) sample A-C after stretching. (d) and (h) present the axial section of (a) and (e), respectively.

During the stretching process, distinct necking appears with a large decrease in thickness of the fiber as shown in Figure 4.2a-c and e-g. Beside the neck region is the shoulder region, which is heated at the beginning but then gets gradually drawn away from the heated region. The rest is stretched but not heated. The thickness of the unheated part is identical to that of the reference samples, which are neither heated nor stretched. The length of the neck region is 3-5 mm. The samples as presented are three typical scenarios (sample A, B and C) we study in this work. The stretching conditions of the three samples are summarized in Table 4.1. The internal structure is investigated by mechanical splitting. Figure 4.2d and h show the axial cross section of a stretched sample and its reference sample. It can be seen that the original microfiber is composed of numerous finer fibers highly aligned in submicron scale, which somehow explains the high k (19 ~ 22 W/m·K) of S-900 fiber. After stretching under the same condition as sample A, the internal structure remains clearly stranded and aligned as well as that of original S-900.

Table 4.1 Stretching conditions and corresponding results for sample A, B and C.

	samples		
	A	B	C
stretching velocity (μm/s)	10	10	20
stretching temperature (°C)	131.5	124.5	116.0
k at RT (W/m·K)	20.7→51.8	20.5→40.5	18.9→34.4
diameter change (μm)	36.0→14.0	42.6→20.7	36.7→23
strain ratio	6.59	4.22	2.55
strain rate (s^{-1})	0.0129	0.0082	0.0155

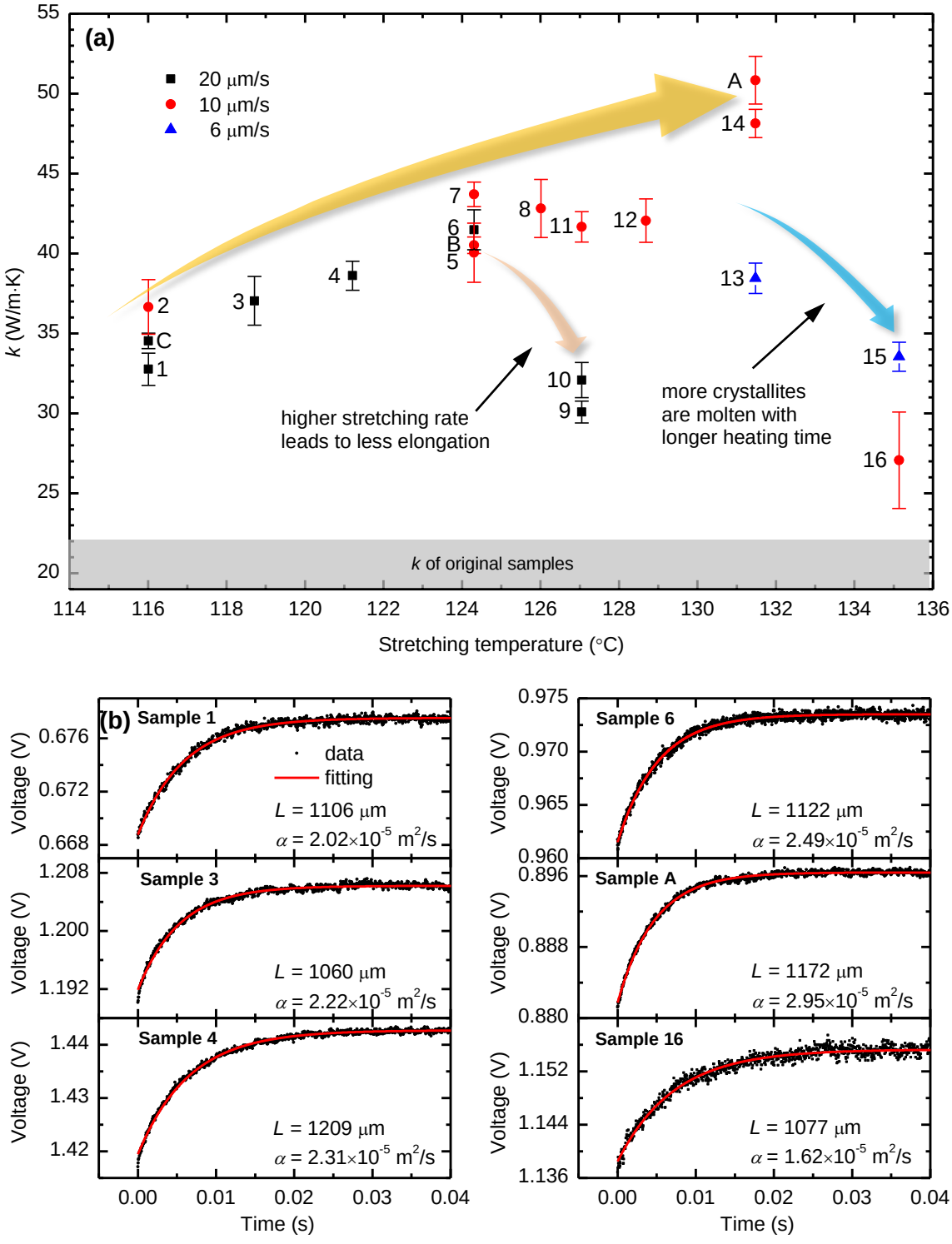

Figure 4.3 Heat stretching and room-temperature thermal characterization. (a) RT *k* of stretched Spectra S-900 fibers with respect to stretching speed and temperature. Besides sample A-C, samples are denoted by numbers. (b) Examples of TET voltage singals

To characterize the thermal properties of stretched Spectra S-900 fibers, we sample the center (3 mm long) of the necked region from stretched fibers. *k* of samples stretched under different conditions is presented in Figure 4.3a, with the fitting quality of thermal characterization shown in Figure 4.3b. There is a clear trend that the *k* increases with increased stretching temperature. *k* increases with increased stretching temperature from 116 ºC to 131.5 ºC as highlighted in the figure. This is due to the longer elongation by stretching (before break) when a higher temperature is used. At 131.5 ºC it reaches a peak. The optimal temperature (131.5 ºC) is very close to 130 ºC, where Smith *et al.* achieved a high degree of orientation for drawn UHMW-PE gel film (strain ratio = 130).[42] Over 131.5 ºC, the heated fiber seems free from stress but it still holds its shape probably due to the extremely long molecular chains of UHMW-PE. The elongation at break and *k* improvement are smaller than those of lower stretching temperature. For example, the sample (Sample 16) stretched at 135 ºC by 3.3 mm has a lower *k* (26.9 W/m·K) than sample A stretched at 131.5 ºC by 5 mm. As the temperature exceeds 135 ºC, the fiber melts before being stretched. The highest *k* value at RT obtained here is 50.8 W/m·K when a fiber stretched at a rate of 10 μm/s at 131.5 ºC (Sample A). Sample A is of great interest and will be studied in detail in the following sections.

As seen in Figure 4.3a, *k* shows a weak dependence on stretching speed. We initially use a relatively fast stretching rate 20 μm/s. When stretching temperature is higher than 124.5 ºC, the elongation at break is significantly reduced compared with that of samples stretched at lower temperature and same speed. This can be clearly proved by the two stretching results at 127 ºC. The two samples (Sample 9 and 10) stretched at 20 μm/s at 127 ºC have a much lower *k* than Sample 11 stretched at 10 μm/s at the same temperature. The overall elongations of these two fibers are both 3 mm, which is considerably shorter than the 5 mm elongation of the fiber

(Sample 11) stretched at the same temperature with a half speed (10 μm/s). It suggests that a high stretching speed might limit the maximum elongation at a threshold temperature, leading to a less improved *k* value. Therefore, a slower stretching rate (10 μm/s) is used for stretching at above 124.5 ºC. As the lower limit, 6 μm/s is tried at 131.5 ºC (Sample 13). However, the *k* value drops a lot. A potential reason is that the lower stretching speed provides longer time for the PE to melt, which weakens the effect of stress.

The strain rate could be a key for the high *k* achieved in this study. It is because the internal tensile stress is related to the strain rate and a moderate level of internal tensile stress could align molecular chains without breaking them. The strain rate used in this work (0.008 ~ 0.016 s^{-1}, 0.0129 s^{-1} for sample A) is close to the range (0.01-0.1 s^{-1}) where optimal chain alignment, crystallinity and elastic modulus were found for stretched UHMW-PE materials. Examples include 0.011 s^{-1}, 0.033 and 0.083 s^{-1} for microfiber (a blend with 2 w% LD-PE), single crystal mat and film, respectively.[21, 43, 44]

CHAPTER 5. IMPROVEMENT OF STRUCTURE IN POLYTHYLENE

This chapter covers the cryogenic thermal characterization and structure analysis of the three representative samples (sample A-C). Various phonon branches are considered in the STD size calculation. XRD and Raman spectroscopy are used to study the structure change in crystalline phase and amorphous phase.

5.1 Thermal Conductivity Behavior under Temperature Variation

After RT thermal characterization, sample A stretched at 131.5 ºC and other two fibers stretched at 124.5 ºC (sample B) and 116 ºC (sample C) are selected for further cryogenic TET measurement. These cryogenic studies are to provide further knowledge how k and α of stretched PE fibers increases over that of un-stretched ones. Also it provides detailed study of the stretching ratio. Properties and elongation details for the samples are listed in Table 4.1. The fiber thickness has already been measured under SEM as shown in Figure 4.2 a-c and e-g.

The cryogenic TET test gives α and k at different temperatures from 30 K to 300 K as shown in Figure 5.1. The data of stretched samples and that of reference samples are compared. k is calculated according to the reported ρc_p.[31] The figures show that, for the stretched and reference samples, α decreases monotonically with increased temperature while k does not. In the plots of k, a subtle decrease against increased temperature near RT could be observed. It is a result of the competition between increasing ρc_p and decreasing α with increased temperature. The increase of ρc_p becomes moderate near RT, which allows $k=\alpha\rho c_p$ to follow the decrease of α. This phenomenon is also observed and discussed in literature.[15-17, 45]

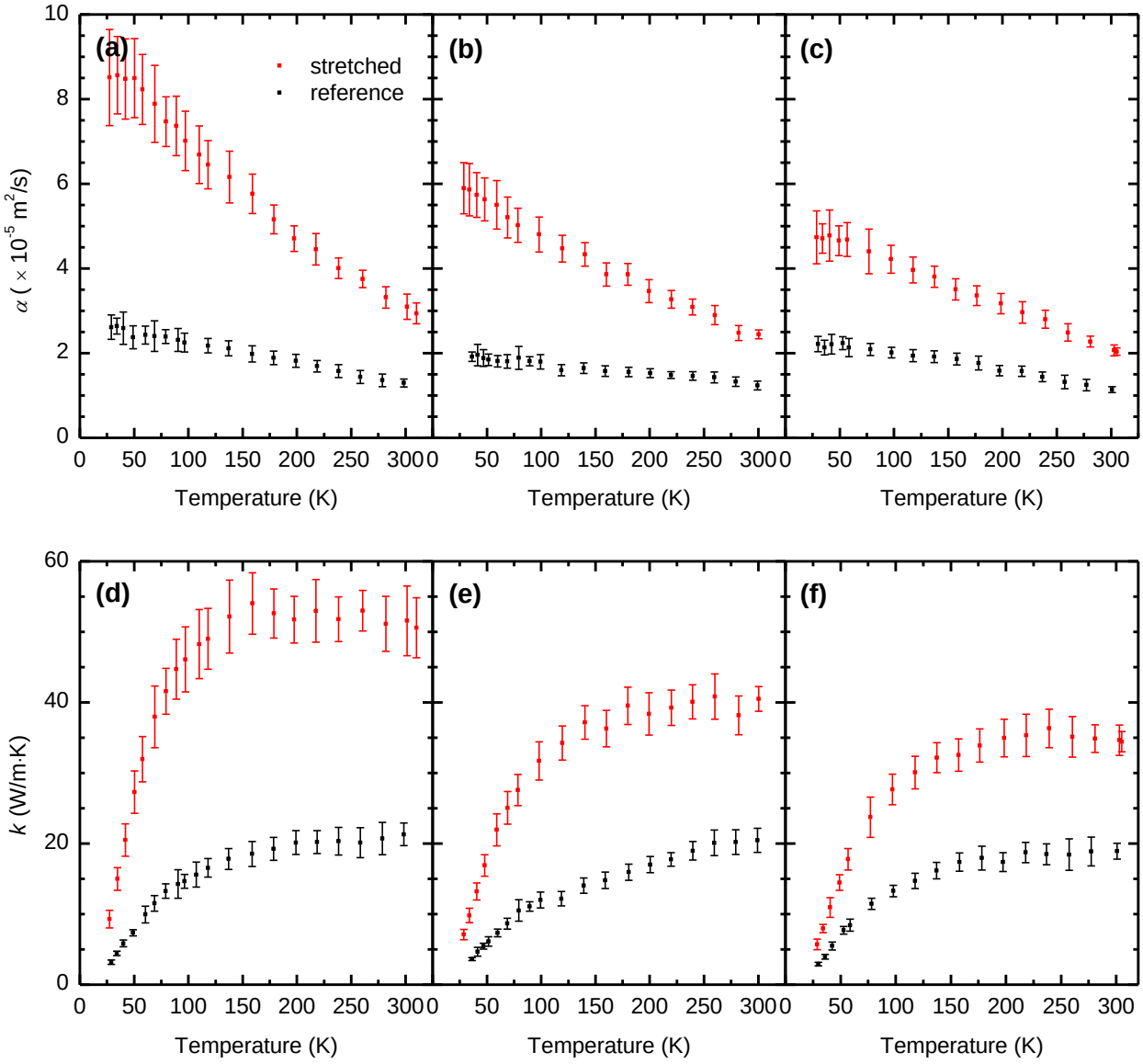

Figure 5.1 α and k against temperature for sample A, B and C. (a), (b) and (c) give α versus temperature for sample A, B and C, respectively. (d), (e) and (f) give the corresponding k against temperature. The error bar represents three standard deviations of the mean for 20 measurements at a temperature.

By comparing the stretched and reference samples, it is observed that not only at RT but also at any temperatures below RT, the stretched samples have much higher k and α. To rule out the effect of difference among un-stretched fibers, we should introduce the k increase ratio k_{str}/k_{ref}, which is the k of stretched sample divided by that of the reference sample. In Figure 5.2, k_{str}/k_{ref}

is plotted versus temperature. As temperature decreases to 30 K from RT, k_{str}/k_{ref} increases from 2.4 to 3.3 for sample A, from 1.5 to 2.8 for sample B, and from 1.8 to 2.5 for sample C. The enhancement of k under cryogenic temperatures is more pronounced.

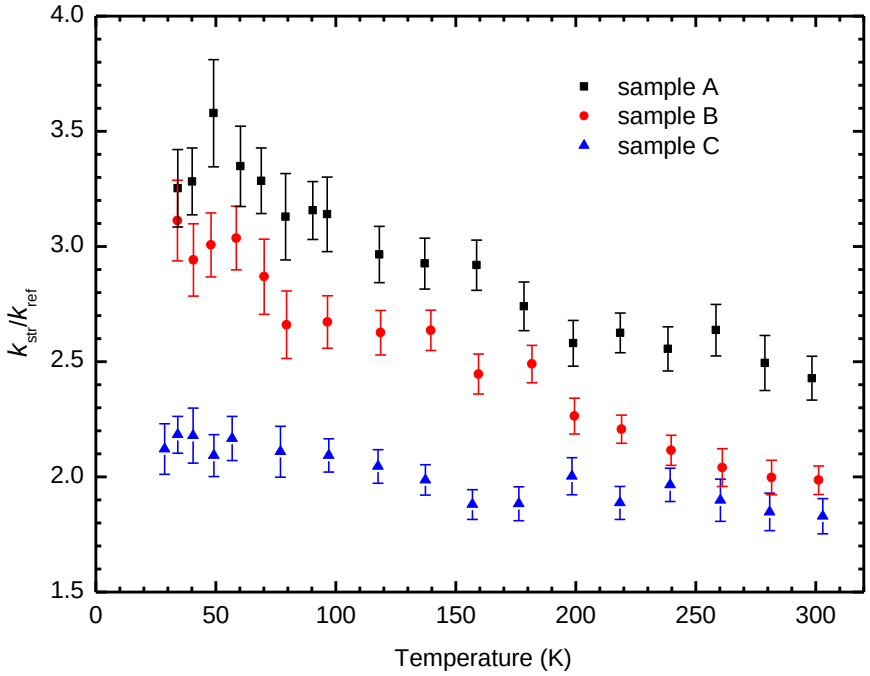

Figure 5.2 k improvement ratio k_{str}/k_{ref} against temperature for sample A, B and C. k_{str} and k_{ref} come from the experimental data from Figure 5.1. The error bar represents standard deviation of the mean.

5.2 Structural Thermal Domain Elongated by Heat Stretching

Based on the measured thermal reffusivity, STD size can be determined for the three selected samples. We can a more accurate description about Θ-STD correlation, considering all phonon dispersion and various phonon branches has been systematically studied by simulation and experiment. The inter-atomic potential used for evaluating phonon behavior is adaptive intermolecular reactive bond order (AIREBO) potential.[40] As $T \rightarrow 0$ K, phonons with different

frequencies are considered to share the same l_0 since only low-frequency/momentum acoustic phonons are excited according to Bose-Einstein distribution. Based on our earlier physics study of Θ_0 of UHMWPE fibers,[3] we have

$$\Theta_0 = \frac{1}{\alpha}\bigg|_{T\to 0} = \frac{\rho c_p}{k}\bigg|_{T\to 0} = \frac{\rho c_p}{\rho c_p v l_0}\bigg|_{T\to 0} = \frac{\sum_{M=1}^{18}\int_0^{\omega_D} \partial U_M / \partial T d\omega}{\sum_{M=1}^{18}\int_0^{\omega_D} \partial U_M / \partial T l_0 v_\omega d\omega}\bigg|_{T\to 0} \tag{6}$$

PE crystals have 4 acoustic phonon branches and 14 optical phonon branches.[4] M denotes the number of phonon branches. U_{M} is the thermal energy for Mth phonon branch, v_ω is the phonon velocity dependent on frequency ω. ω_D is the cutoff frequency for each phonon branch. For acoustic phonon branches, the thermal energy U_M is given as:

$$U_M = \int g(\omega) n(\omega) \hbar\omega d\omega = \int_0^{\omega_D} g(\omega)\left(\frac{\hbar\omega}{e^{\hbar\omega/k_B T} - 1}\right) d\omega \tag{7}$$

where $g(\omega)$ is the density of state. The volumetric heat capacity C_a for the acoustic phonons is

$$C_a = \sum_{M=1}^{4}\int_0^{\omega_D} \partial U_M / \partial T d\omega = \sum_{M=1}^{4}\int_0^{\omega_D} g(\omega) k_B \left(\frac{\hbar\omega}{k_B T}\right)^2 \frac{e^{\hbar\omega/k_B T}}{(e^{\hbar\omega/k_B T} - 1)^2} d\omega \tag{8}$$

For optical phonons, the thermal energy is given by the Einstein model： $U = N < n > \hbar\omega$, among which N is the number of primitive cells. Thus we have

$$C_o = \sum_{M=5}^{18}\int_0^{\omega_D} \partial U_M / \partial T d\omega == \sum_{M=5}^{18} N k_B (\frac{\hbar\omega}{k_B T})^2 \frac{e^{\hbar\omega/k_B T}}{(e^{\hbar\omega/k_B T} - 1)^2} \tag{9}$$

The total volumetric heat capacity is the combination of two kinds of phonons. The accuracy of this heat capacity calculation is evaluated by comparing with experimental results.[5] With the physics that the optical phonons have almost zero phonon velocity, acoustic phonons are the major heat carriers in the thermal transport in polymers. Therefore, optical phonon contribution is neglected in the thermal conductivity term. Combining substituting eqn. 8 and 9 in to eqn. 6, we have:

$$\Theta_0 = \left. \frac{\sum_{M=1}^{4} \int_0^{\omega_D} g(\omega) k_B (\hbar\omega / k_B T)^2 e^{\hbar\omega/k_B T} / (e^{\hbar\omega/k_B T} - 1)^2 d\omega + \sum_{M=5}^{18} k_B (\hbar\omega / k_B T)^2 e^{\hbar\omega/k_B T} / (e^{\hbar\omega/k_B T} - 1)^2}{l_0 \sum_{M=1}^{4} \int_0^{\omega_D} g(\omega) k_B (\hbar\omega / k_B T)^2 e^{\hbar\omega/k_B T} / (e^{\hbar\omega/k_B T} - 1)^2 v_\omega d\omega} \right|_{T \to 0}$$

(10)

With eqn. 12, STD size (l_0) can be determined with the knowledge of Θ_0, $g(\omega)$, and v_ω. The dependence of $g(\omega)$ and v_ω on ω has been given and discussed in literature.[3]

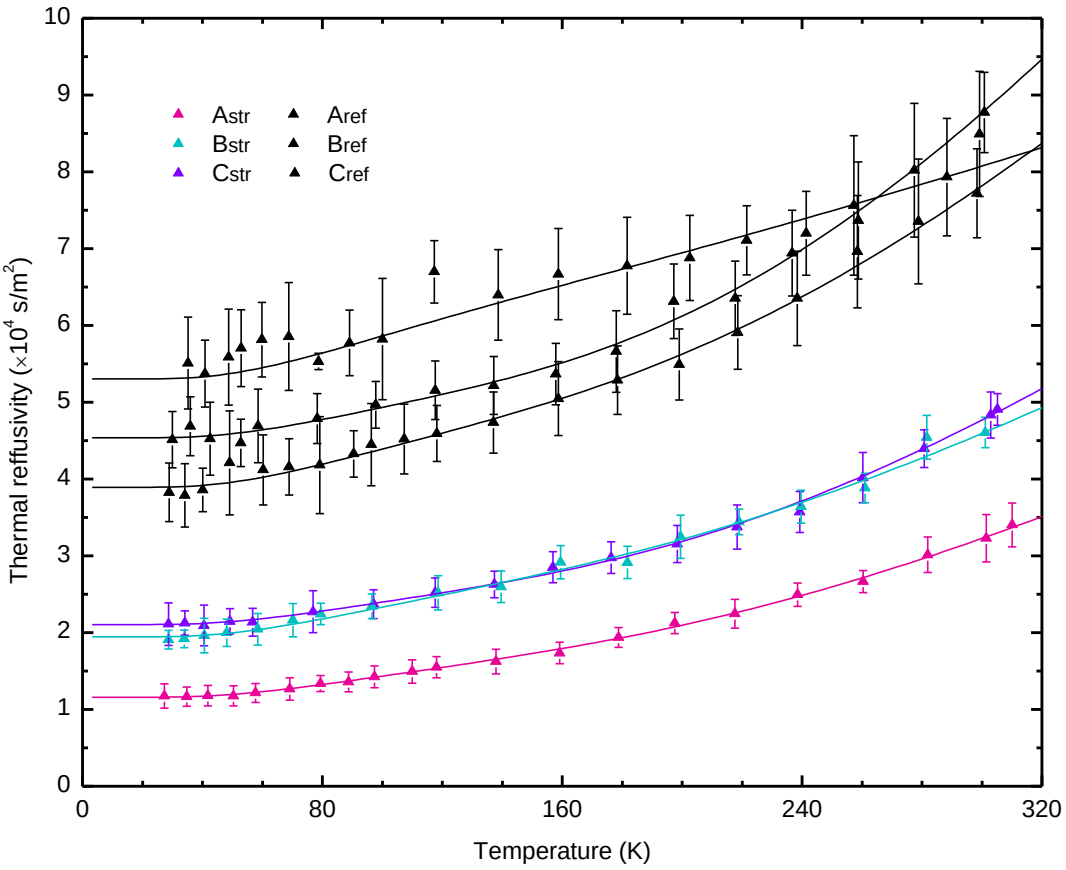

Figure 5.3 Θ against temperature for sample A, B and C. Reference samples and stretched samples are denoted by "ref" and "str", respectively. Each data point is a mean value of 20 repeated measurements. The error bar represents three standard deviations of the mean.

Based on the effective Θ_0 shown in Figure 5.3, STD sizes of un-stretched UHMW-PE fibers are determined to be 7.35, 5.47 and 6.19 nm for sample A, B and C, respectively. Through heat stretching, their l_0 rises up to 24.82, 14.95 and 13.63 nm. Those enlarged STD sizes indicate reduced level of phonon-boundary scattering. Here, the amorphous phase is considered as defect in crystals. The other way to calculate STD size is ruling out the contribution of amorphous phase to Θ, which is more physically meaningful. The crystallinity change given by XRD analysis is from 92.09% to 82.54% for the optimum sample (sample A). Based on the crystallinity and effective medium approximation, the stretching-induced STD size change in sample A is evaluated to be from 9.81 nm to 46.71 nm. The significantly reduced level of defect-phonon scattering proposes a structure change, which favors phonon transport. This will be explained by the following structural characterization.

5.3 Raman Scanning along Sample

Raman spectroscopy (confocal Raman system, Voyage, B&W Tek, Inc.) is used to characterize the structure change along a stretched sample. The sample is a duplicate of sample A. Laser beam (532 nm in wavelength, 16 mW in laser power) scans from the center of heated region to the unheated region. The polarization of laser is parallel to the fiber axis. A series of Raman spectra are produced as shown in Figure 5.4a. The anti-symmetric (1060 cm^{-1}) and symmetric (1130 cm^{-1}) C-C stretching bands represent vibration of skeletal chains parallel and perpendicular to the chain axis, respectively. The band area ratio between the two bands does not change at different positions, which suggests consistent molecule alignment along a stretched fiber.

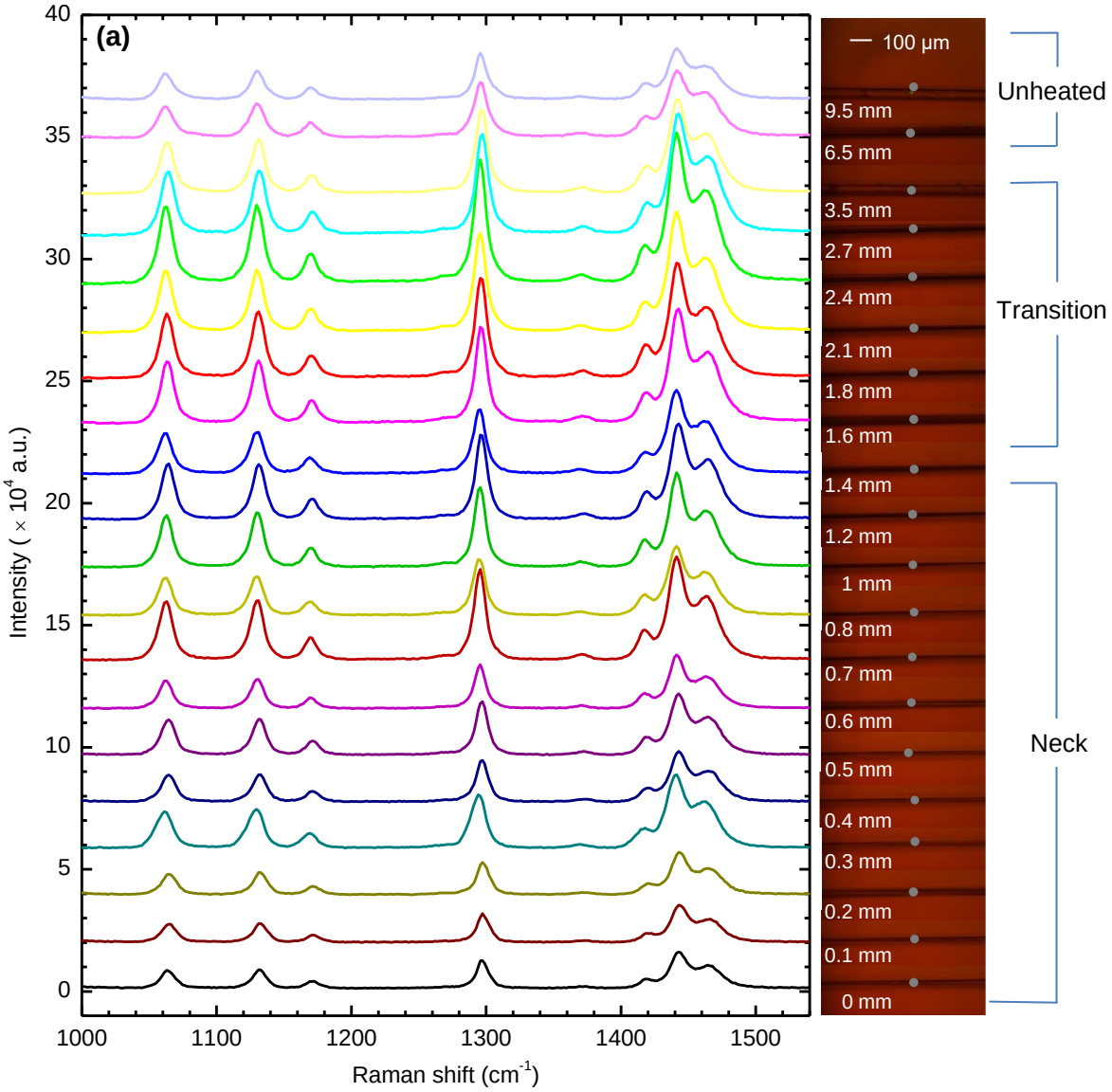

Figure 5.4 Raman spectra collected along sample A. (a) Raman spectra obtained at different positions along the sampled UHMW-PE fiber. The distance of the beam spot from the center of the neck region is presented on the right for each spectrum, with a microscope image. Beam spots are marked with grey spots. The integration time is 6 s for the unheated region and 10 s for the rest. (b) FWHM of peaks at 1296, 1440 and 1460 cm^{-1} (c) Peak area ratios, including $A_{1296}/(A_{1440}+A_{1460})$ and A_{1440}/A_{1460}.

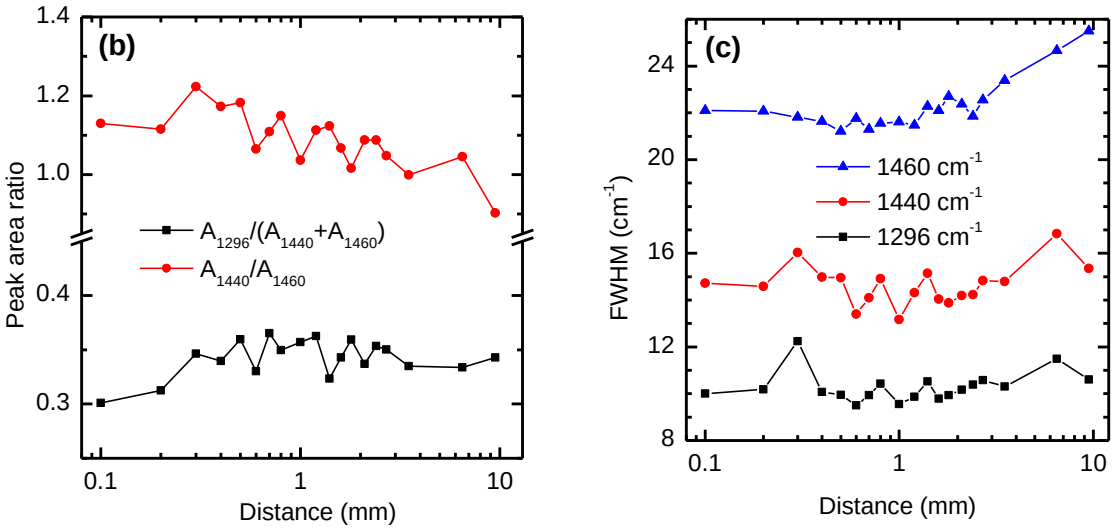

Figure 5.4 (continued)

The peak at 1296 cm^{-1} stands for CH_2 twisting mode. The sharp peak at 1416 cm^{-1} suggests the dominance of orthorhombic crystalline structure. The splitting peaks at 1440 and 1460 cm^{-1} stand for CH_2 bending vibration in interfacial (between amorphous phase and crystallites) amorphous chains and melt-like amorphous chains, respectively. Therefore, we can use the peak area ratio $A_{1296}/(A_{1440}+A_{1460})$ to evaluate crystallinity and A_{1440}/A_{1460} evaluate the composition of amorphous phase. Figure 5.4b shows insignificant variation for both peak area ratios. In Fig. 5.4c, no obvious change in the full width at half-maximum (FWHM) is observed for the peaks at 1296 and 1440 cm^{-1} and 1460 cm^{-1}. This measurement is limited by the curved surface of fiber because the peak width and intensity could fluctuate when the laser spot on the surface slightly moves.

5.4 Crystallinity and Crystallite Size and Orientation: Effect of Heat Stretching

5.4.1 Crystallite alignment

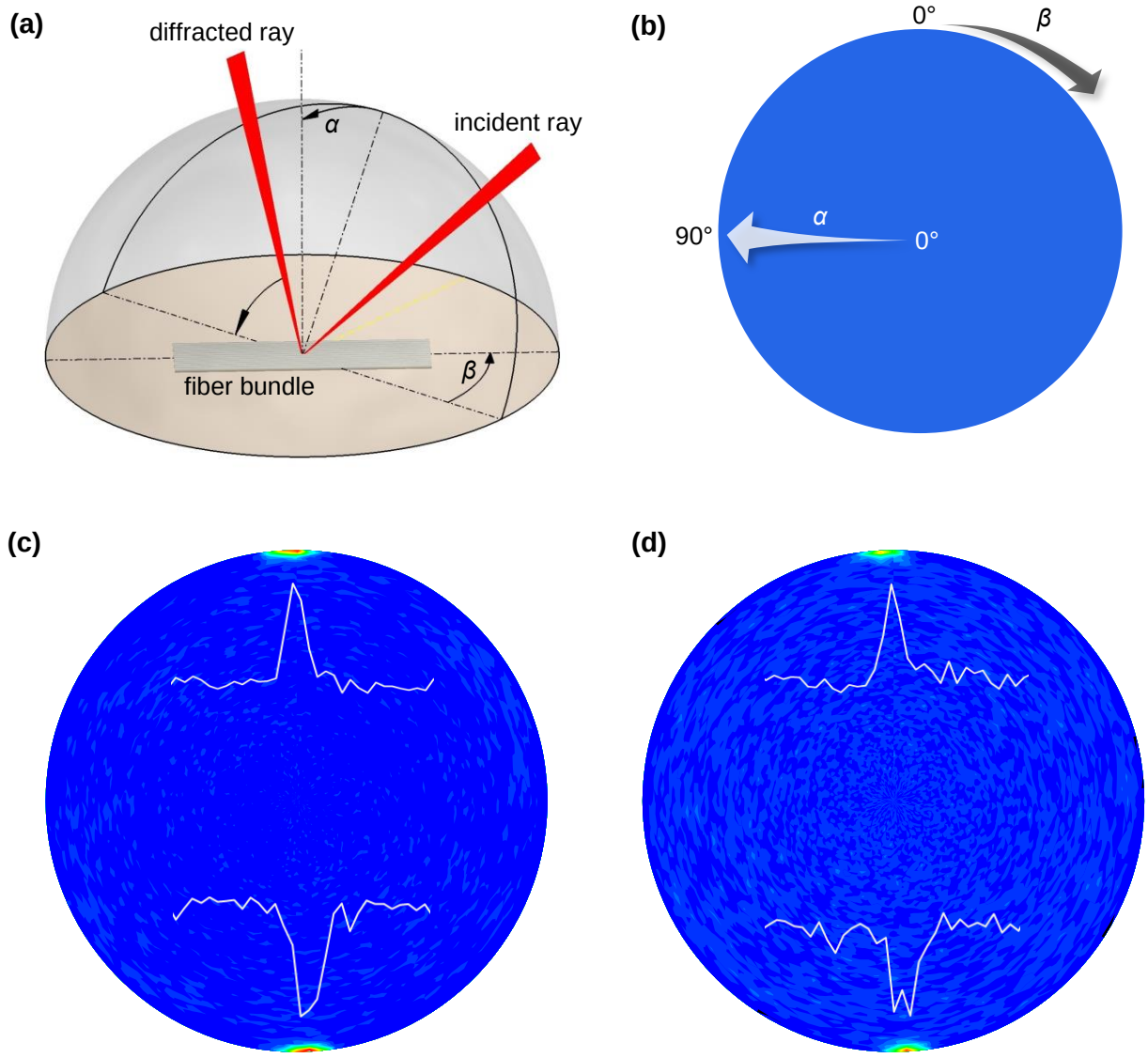

Figure 5.5 XRD pole figure analysis. (a) Schematic of XRD pole figure scanning for aligned fiber bundle. (b) Definition of α and β in the scanning pattern. XRD pole figure for (002) of the reference sample. (c) XRD pole figure pattern for the (002) plane of original Spectra S-900 (d) XRD pole figure pattern for the (002) plane of Spectra S-900 stretched under the sample condition as sample A. The inset spectra represent local intensity variation of β scan.

To investigate the alignment of crystallites, XRD pole figure is used to characterize the orientation of (002) planes within the fibers, considering that (002) planes are perpendicular to the backbone chain of polyethylene. Samples include 50 original Spectra S-900 fibers and 50 S-900 fibers stretched under the same condition as sample A. Both groups are aligned as a bundle and spread evenly in the form like a 30 mm × 1.5 mm thin film. The x-ray beam approximately covers 1 mm × 1 mm area on the bundles. With the configuration as shown in Fig. 5.5a-b, we were able to collect the pole figure patterns (XRD, Rigaku Smartlab diffractometer) patterns as shown in Fig. 5.5c-d. The two strong peaks at α = 0° and β = 0°/180° has been found for both samples. The FWHM of the peaks in β scan (inset spectra in Fig. 5.5c-d) are 10.4° and 8.02° before stretching. After stretching, they are 10.5° and 7.1°. This suggests that the carbon chains in crystalline phase have already been highly oriented to the fiber axis before stretching and heat stretching does not create observable change to the alignment of crystallites.

5.4.2 Crystallite size

The XRD patterns (Bruker D8 Discover, Cu Kα source) for the fiber bundles are also given as shown in Figure 5.6. Based on the fitting of peak breadth, the crystallite sizes are determined to be 17.5 nm for (200) planes and 18.28 nm for the (002) plane after stretching. For the reference sample, the crystallite sizes are 17.4 nm and 18.3 nm for (200) plane and (002) plane, respectively. Those results indicate the crystallite size has not been changed by stretching.

In addition, a new peak at the band of (010) plane is observed after heat stretching. The new peak suggests the presence of monoclinic/triclinic crystals, probably due to introduction of stress during stretching or recrystallization.[46, 47]

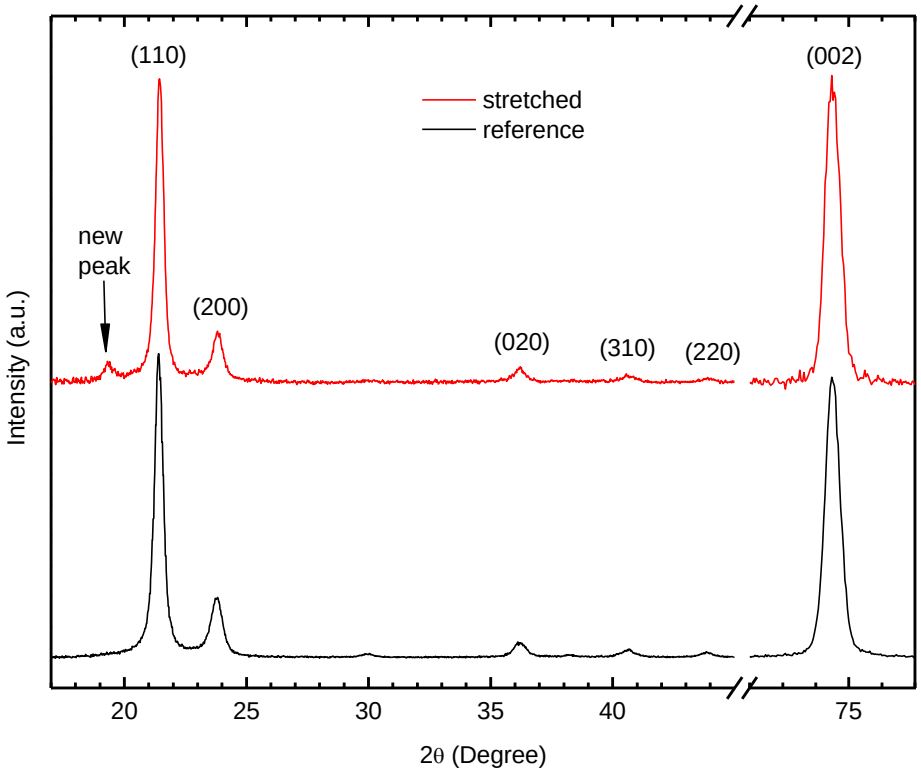

Figure 5.6 XRD pattern of the UHMW-PE fiber bundles. The pattern between 17 and 45 degrees are obtained by out-of-plane x-ray beam. The (002) peak around 75 degrees is obtained by in-plane x-ray beam. They are plotted in the same figure for brevity.

The crystallinity calculated from peak breadth decreases from 92.09% to 82.54% after stretching. The crystallinity of original fiber agrees well with our previous measurement (91.9%).[31] However, the decreased crystallinity after stretching is definitely out of expectation because it seems contrary to the *k* increase, given the crystallite size and orientation are not changed. We speculate the observed significant *k* increase is more induced by the restructuring in amorphous phase.

5.4.3 Crystallinity reduction and structure physical model

Based on the structure characterization, the reconstructuring could happen in two ways. The first possibility is the relocation of amorphous structures. A two-dimensional composite

model is used to explain the effect of amorphous relocation. UHMW-PE microfiber has a composite structure formed by aligned crystallites embedded in amorphous matrix as shown in Figure 5.7 (a).[48] ϕc, ϕa,⊥ and ϕa,// are volumetric fraction of crystallites, serially connected amorphous phase (blue region) and parallel connected amorphous phase, respectively.

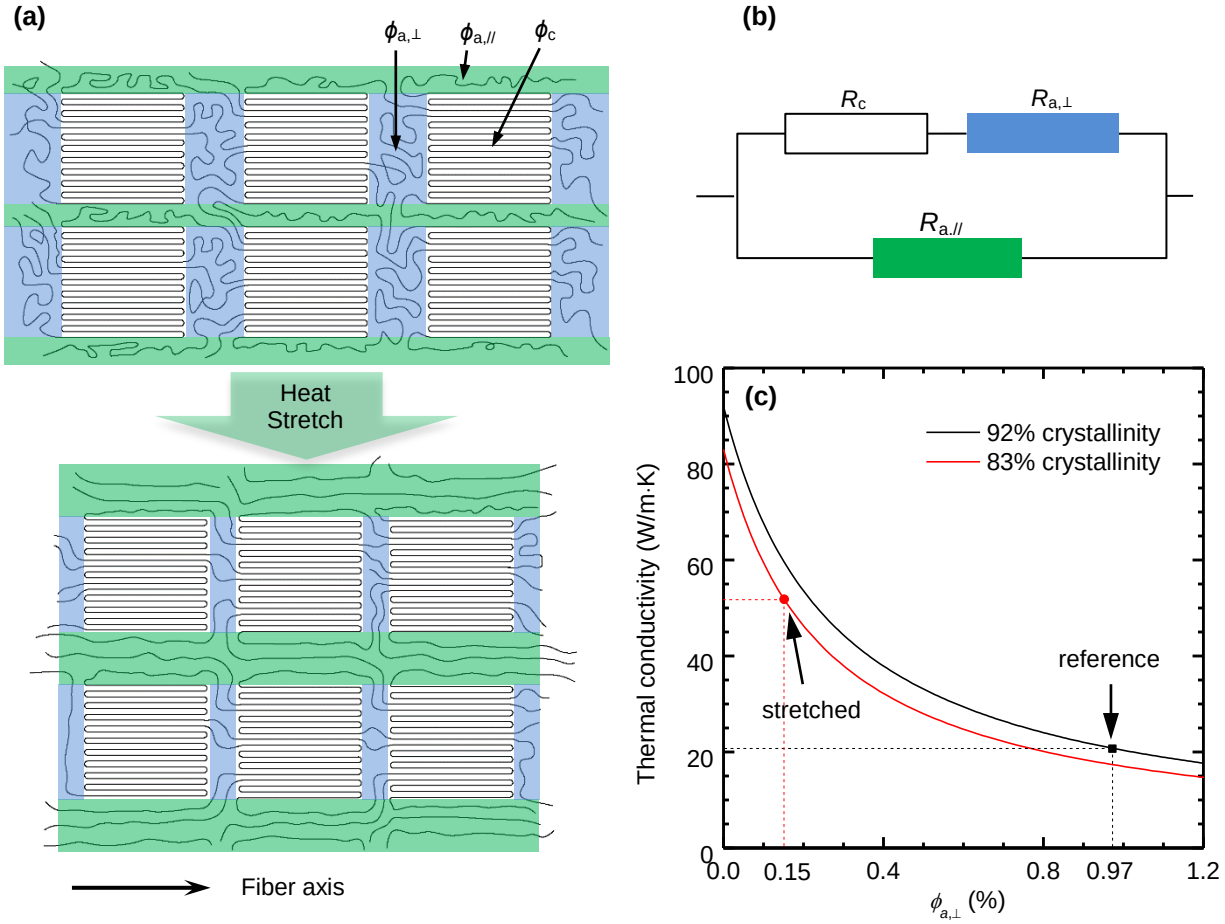

Figure 5.7 Proposed physics model: (a) Structural model of UHMW-PE fiber before and after heat stretching, with fiber axis in the horizontal direction. The volumetric fractions are denoted by $\phi_{a,\perp}$, $\phi_{a,//}$, and ϕ_c for serial amorphous regions, parallel amorphous regions and crystalline regions respectively. (b) Thermal resistance network model for thermal transport along fiber axis. $R_{a,\perp}$, $R_{a,//}$ and R_c are the thermal resistances of serial amorphous region, parallel amorphous region and crystalline region, respectively. For a sample of unit length and unit cross-sectional area, $R_{a,\perp} = \phi_{a,\perp} / [\kappa_a (\phi_{a,\perp} + \phi_c)^2]$, $R_{a,//} = 1/\kappa_a \phi_{a,//}$, $R_c = \phi_c / [\kappa_a (\phi_{a,\perp} + \phi_c)^2]$, and $1/R_{eff} = 1/R_{a,//} + 1/(R_{a,\perp} + R_c)$. (c) Thermal conductivity variation against the fraction of serially connected amorphous region. The two data points come from *k* measured by TET and the crystallinity characterized by XRD.

Here we assume 1) the amorphous phase is homogeneous: ka,⊥ = ka,// = ka; 2) ka and kc remain unchanged during heat stretching. Then the effective thermal conductivity k_{eff} in fiber axis can be calculated based on the thermal resistance network model as shown in Figure 5.7(b): $\kappa_{eff} = (1-\phi_{a,//})^2 \kappa_c \kappa_a / (\phi_c \kappa_a + \phi_{a,\perp} \kappa_c) + \phi_{a,//} \kappa_a$. The XRD analysis gives ϕc ≈ 92% before stretching and ϕc ≈ 83% after stretching. To proof the existence of parallel connected amorphous phase, we propose that there is no amorphous structure parallel connected with crystalline structure. In other words ϕa,// = 0 for the original PE fiber. Then even if kc and ka are taken as the highest experimental values to our knowledge: kc = 100 W/m·K and ka = 0.3 W/m·K,[27, 49] for original fibers the calculated value keff ≈ 3.6 W/m·K is still fairly lower than the measured value 21.3 W/m·K. This contradiction denies the assumption that ϕa,// = 0, suggesting the existence of parallel connected amorphous region. Then we can calculate ϕa,// based on the measured k value of sample A. Before stretching, ϕc ≈ 92% and keff = 21.3 W/m·K. The ϕa,// value is determined to be ~ 7.06% and ϕa,⊥ ≈ 0.94%. As for the stretched fibers given ϕc ≈ 83% and k = 51.8 W/m·K, ϕa,// ≈ 16.84% and ϕa,⊥ ≈ 0.16%. Based on the two-dimensional polymer composite model, we find that k is highly sensitive to ϕa,⊥. The sensitivity is presented in Figure 5.7(c). The model presents a possibility that the 140% k improvement in experiment could be caused by an increase of ϕa,⊥ by merely 0.78%.

This first case could be supported by a bending test. A stretched fiber and an original fiber are bent repeatedly. The stretched fiber is stretched under the same condition as sample A. The test shows that a rugged surface appears on the stretched fiber after repeated bending while the original fiber still has a smooth and aligned surface as before bending. (Fig. 5.8)

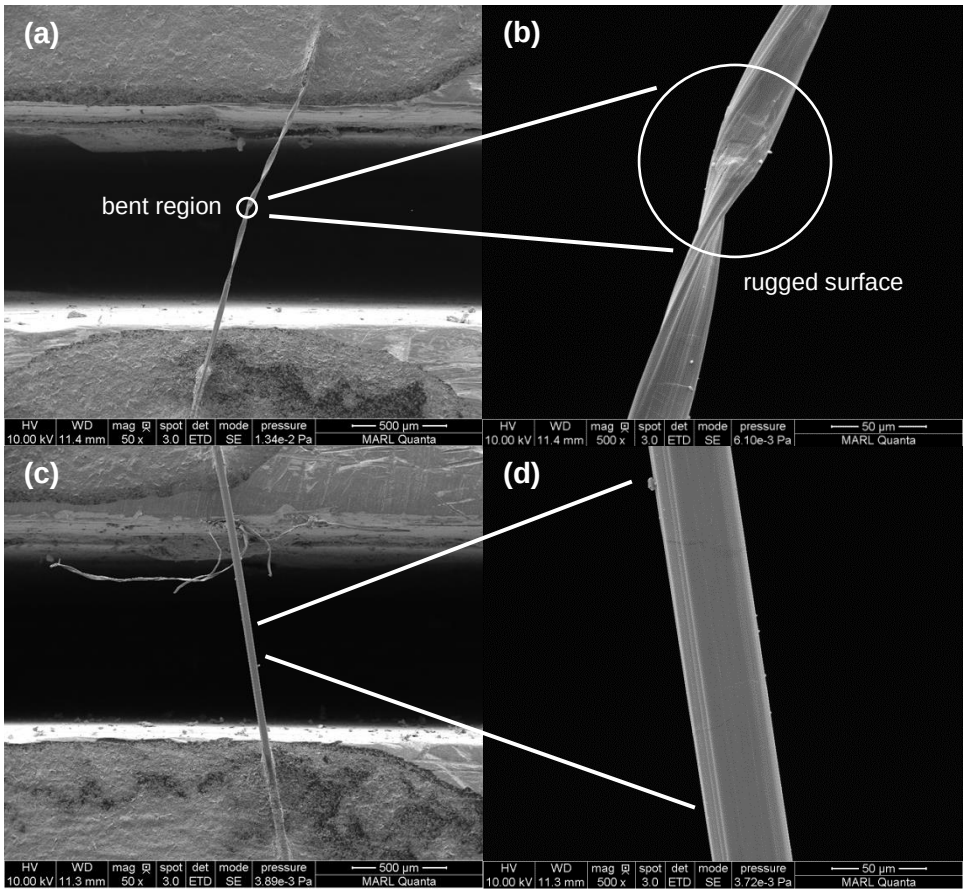

Figure 5.8 SEM images of the UHMW-PE fibers after repeated bending. (a) A sample that is stretched under the same condition as sample A and bent for several times. The bent part locates in the middle of the gap. (b) The surface of the bent part of the sample in (a). The surface turns from a smooth and aligned shape to a rugged shape, indicating the occurrence of irreversible deformation during bending. (c) An original sample after being bent repeatedly. (d) The bent part of the original sample. It is hard to find where it is bent from the image. The bending test indicates that the UHMWPE loses some elasticity during heat stretching, which is potentially resulted from the reduced fraction of serially connected amorphous structure.

The rugged surface suggests the occurrence of plastic deformation in the bent region. The UHMWPE fiber could lose some elasticity during heat stretching, potentially resulted from the reduced fraction of serially connected amorphous structure. For instance, if there is no serially

connected amorphous structure, the crystalline part could be more easily bent to have plastic change or to break.

Due to the difficulty in observing the spatial distribution of amorphous phase, this possibility cannot be fully supported by experimental evidence. However, it should be considered and worth attention in the future research. Because it is possible that reducing amorphous phase is not an effective practice to achieve high thermal conductivity.

5.4.4 Polarized Raman spectroscopy

The second possibility is the improved alignment of amorphous phase. It has been documented that the amorphous structure could be partially aligned to the stretching direction during mechanical stretching.[50, 51] If the alignment of amorphous chains occurs, k of amorphous phase should be enhanced and further lead to an increase in overall k. To understand the chain alignment, polarized Raman spectroscopy is employed by adding a polarizer to the laser source. The detector is not polarized. The laser beam is focused on the center of the stretched section of an optimum sample. During measurement, spectra are collected with different angle between polarization and fiber axis (γ). A spectrum is collect each time when γ is changed by 10°. An offset view of collected spectra is presented in Figure 5.9(a).

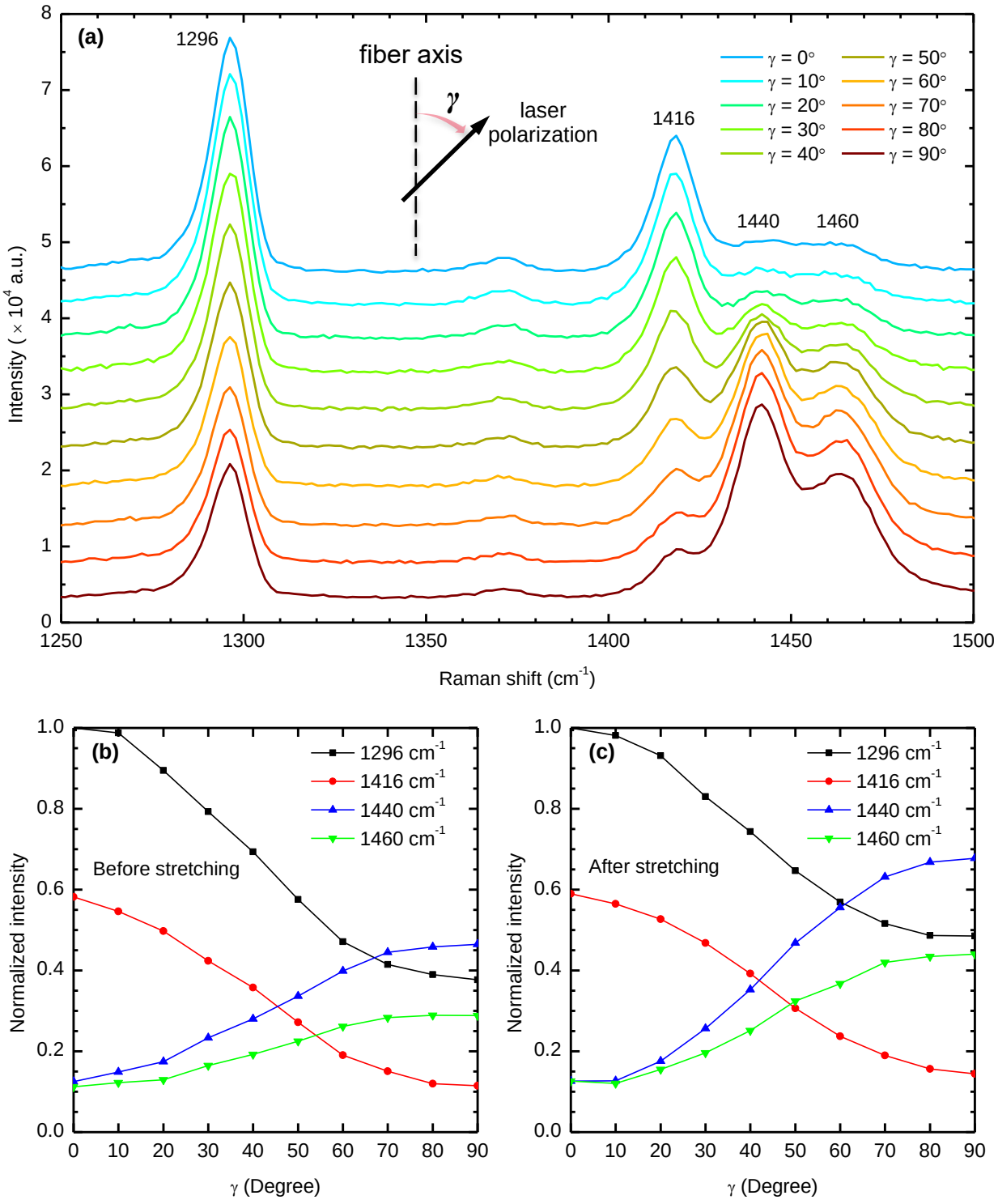

Figure 5.9 Polarized Raman spectroscopy of sample A. (a) Raman spectra of stretched sample A with respect to varied γ, the angle between fiber axis and laser polarization. (b) (c) Normalized Raman peak intensity versus γ for the sample A before and after stretching, respectively. The caliber of normalization is the intensity of 1296 cm^{-1} when $\gamma = 0°$.

It is observed that, when polarization comes to be parallel to the fiber, two crystalline bands (1296 cm^{-1} and 1416 cm^{-1}) rise while the two amorphous bands (1440 cm^{-1} and 1460 cm^{-1}) drop.[52] Based on the knowledge that the vibration related to the two crystalline bands is along c-axis (along the zig-zag molecular chain) and the vibration of the two amorphous bands is perpendicular to c-axis, it is conclusive that the chains in both amorphous region and crystallites are partially aligned along the fiber axis.

The influence of heat stretching on chain alignment is evaluated by comparing the anisotropy of the four peaks. The peak intensity change with respect to γ is presented in Figure 5.9b-c The internal intensity standard is set as the intensity of 1296 cm^{-1} band at $\gamma = 0°$. All the intensities are normalized by the standard for convenience of comparison. It can be observed that the anisotropy of amorphous structure increases significantly while the anisotropy of crystalline structures decreases slightly. Specifically, for γ from 0° to 90° the intensity drop of 1296 cm^{-1} band decrease from 60% to 50% after stretching, indicating a reduced structure anisotropy for crystalline phase. This change is not reflected by the XRD pole analysis, potentially due to its insignificance. Then we compare the intensities of the four peaks at a certain γ. As $\gamma = 0°$, the relative intensities of amorphous peaks remain unchanged before and after stretching although the amorphous fraction increases after stretching according to XRD analysis. This proposes a reduced fraction of unaligned amorphous structures in the amorphous region since the crystalline fraction decreases after stretching. As $\gamma = 90°$, stronger bands for parallel amorphous structure and perpendicular crystallites alignment is found. It indicates that unaligned crystallites and aligned amorphous structure increases in quantity after stretching. As we indicated above, the reduction in the alignment in the crystalline structure is rather trivial. But the alignment improvement in the amorphous structure is more obvious. After stretching, the anisotropic ratio

of CH_2 bending vibration near 1440 and 1460 cm^{-1} have an intensity increase of 536% and 348% , respectively, when γ changes from 0° to 90°. Before stretching, this increase is only 372% and 257%, respectively. The amplified anisotropic nature of bending vibration in amorphous chains suggests that amorphous chains are more aligned to the fiber axis, which can lead to a substantial enhancement in *k*.

In conclusion, the polarized Raman study shows that the amorphous chains turn to be more aligned although some crystallites become less aligned. The high *k* (~350 W/m·K) of a single PE molecular chain suggests a great potential for *k* enhancement by aligning carbon chains. It allows more heat load be transferred by the backbones of PE in the same direction. This will significantly reduce the huge thermal resistance of the amorphous structure among crystallites in the axis direction, leading to a significant *k* enhancement in overall.

Besides the two possible cases based on experimental evidence, there is a third case, which is possible but not covered by the experimental study in this work. Remind that the stretching process ends with quenching in ambient air. The cooling process could end in 1-2 seconds. During cooling, a temperature gradient should exist along the fiber, with highest temperature in the center. Temperature gradient can guide the orientation of growing crystalline lamellae. However, the recrystallization could be stopped on its half way, which makes the crystal melts stay amorphous in terms of XRD analysis. The partial melting of crystalline phase allows the chain movement, which functions together with the temperature gradient to make an overall improved alignment. The increased amorphous fraction should come from the molten crystals, which might sustain better heat conduction but not be detectable by XRD.

CHAPTER 6. STRUCTURAL THERMAL DOMAIN IN SILICON CARBIDE MICROWIRES

This chapter covers a comparative study on the thermal properties and the structures of a series of advanced SiC microwires to provide the first-hand insight into the structure and thermal properties of nanocrystalline SiC, and to uncover the effect of structure on thermal transport capacity. Samples include Sylramic and Hi-Nicalon S fabricated by conversion of polymer precursors and LCVD-FFF fabricated by laser-driven chemical vapor deposition (LCVD).[53, 54] Their structure is characterized by XRD and Raman spectroscopy.

6.1 Samples

The samples measured in this study include three 3C-SiC nanocrystalline microfibers: Sylramic, Hi-Nicalon S and LCVD-FFF. Sylramic (developed by Dow Corning and manufactured by COI Ceramics) is fabricated by the conversion of polytitanocarbosilane (PTC) precursor followed by pyrolysis in hydrogen with boron as additive.[55] Hi-Nicalon S (from Nippon Carbon) is fabricated by electron-beam curing of polycarbonsilane (PCS) precursor followed by pyrolysis in hydrogen gas.[54] Both polymer-based fibers feature dominant 3C-SiC phase, near-stoichiometric composition (Si/C at. % = 0.95-1, excessive carbon in the core),[56] low oxygen content (<1 wt. %) and low porosity.[57] The drawback of the polymer-based technique at the current stage is that the as-produced SiC microfibers have not been cost efficient and contain free carbon in the core or residual of additives.[55, 57, 58] LCVD-FFF from Free Form Fiber is fabricated by the LCVD process. In general, the growth of the microwire on a substrate is initiated by a laser beam, which provides the energy to break apart the gas precursors and leads to the gas-phase reaction to form the solid deposit. The LCVD-based fiber features

reduced fabrication cost and high purity of the fiber core, but has excessive silicon near periphery (a characteristic of CVD process for SiC[59]) and reduced grain size, which will be discussed in section 6.1.

6.2 Structure Analysis

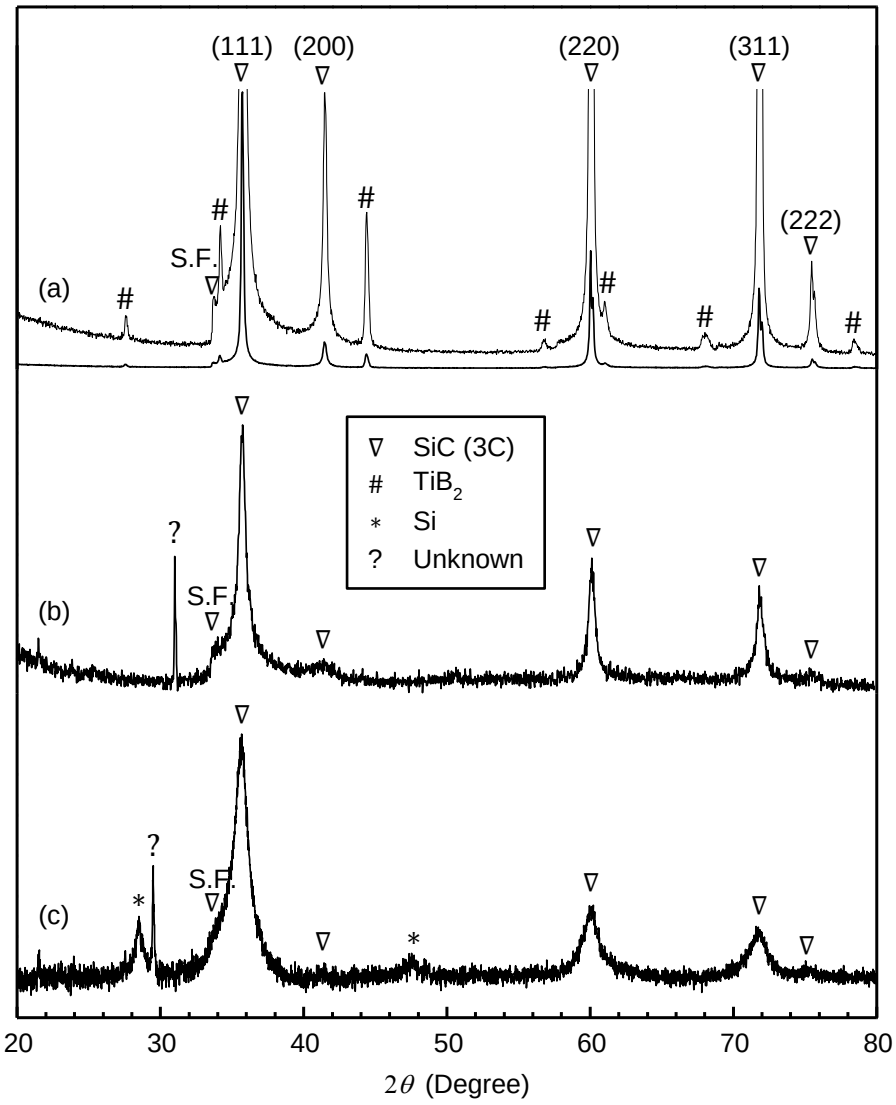

Figure 6.1 XRD patterns of Sylramic (a), Hi-Nicalon S (b) and LCVD-FFF (c). An offset and enlarged view is provided for Sylramic. The sharp peaks besides (with less than half degree shift) the (220) and (311) peaks of SiC in Sylramic could be related to titanium carbide.[60] S.F. denotes stacking faults in 3C-SiC.[61] The baseline of (c) has been subtracted.

XRD (Cu-Kα source, λ = 0.15418 nm) spectra were recorded by a Bruker D8 Advance diffractometer for a sample fiber bundle that had been attached to a zero-background holder with Vaseline. The incident beam is parallel with the fibers, pointing to the cross section. The XRD results are shown in Fig. 6.1. The diffraction intensity versus diffraction angle (2θ) confirms that the main phase of the samples is 3C–SiC, indicated by the (111) peak (d = 0.251 nm, 2θ = 35.7°), (220) peak (d = 0.154 nm, 2θ = 60°) and (311) peak (d = 0.131 nm, 2θ = 71.8°). The crystallite size l_{XRD} determined by the breadth of XRD peaks is 67-114, 14-19 and 6-8 nm for Sylramic, Hi-Nicalon S and LCVD-FFF, respectively. l_{XRD} of Sylramic and Hi-Nicalon S is consistent with previous measurement by both XRD and transmission electron microscope.[55, 62] The specific l_{XRD} values for different 2θ are shown in Table 4.1. It is seen the grains in Hi-Nicalon S and LCVD-FFF SiC fibers have a low aspect ratio in its geometry, and the grain in Sylramic SiC fibers are shorter in the (111) direction, suggesting an oval shape. Note that the instrumental broadening (β_{ins}) has been estimated as a constant 0.07°, which could result in an underestimation of β_{ins} for the (311) peak. Besides the SiC peaks, the presence of substantial titanium diboride (TiB_2) and trivial titanium carbide (TiC) in Sylramic is assigned to the titanium precursor additive and boron sintering additive.[55] The unknown phase (2θ = 31°) in Hi-Nicalon S is possibly related to fine quartz,[63, 64] considering the oxygen content has been found by Auger electron spectroscopy.[56] For LCVD-FFF, the silicon peaks are related to the excessive silicon content due to CVD processing. Quantitative phase analysis for LCVD-FFF presents 92.7 wt. % of 3C-SiC, 5.3 wt. % of Si and 2 wt. % of unknown phase (2θ = 29.6°).

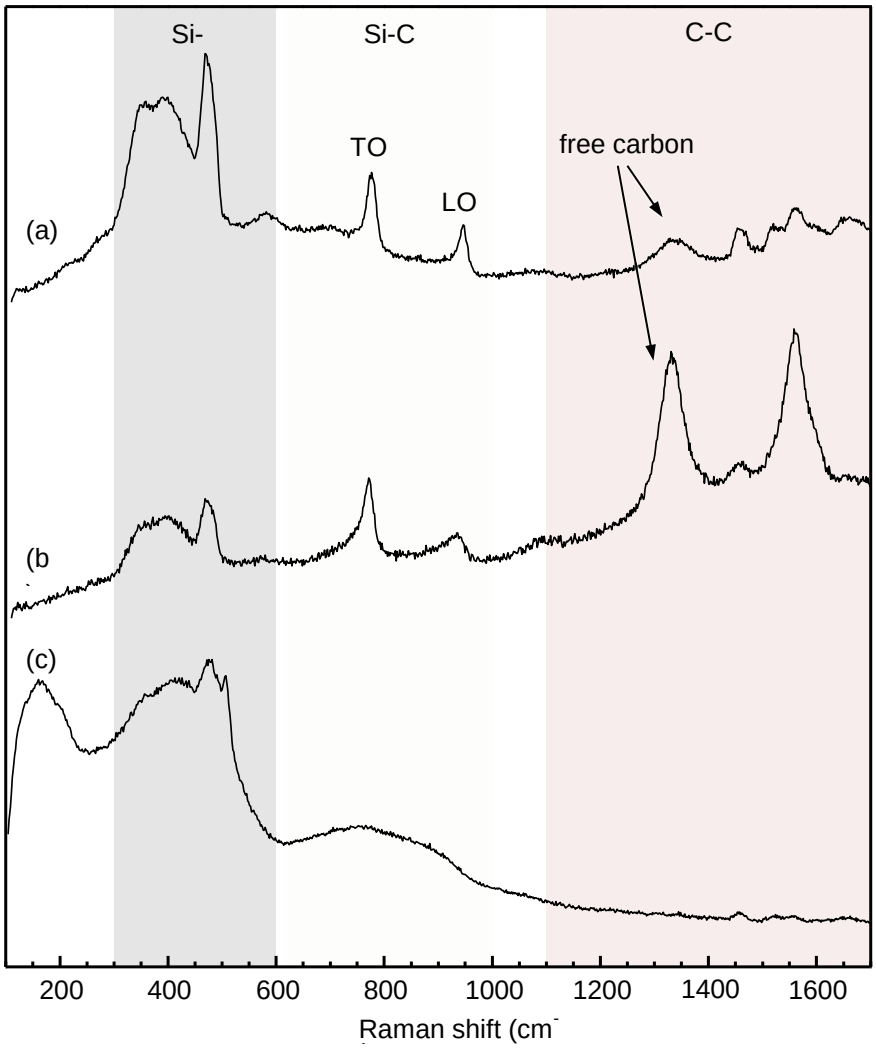

Figure 6.2 Raman spectra obtained at the core of Sylramic (a), Hi-Nicalon S (b) and LCVD-FFF (c). The peaks for Si-Si, Si-C and C-C vibration modes are located in the range of 300-600, 600-1000 and 1100-1700 cm^{-1}, respectively.

Raman spectroscopy was performed at room temperature using a confocal Raman system with back-scattering configuration. A green laser (λ = 532 nm) beam was focused on the center of the cross section of the sample fiber. The focal spot size was restricted to 2.5 μm in full width at half maximum by passing the incident beam through a 20× lens. The laser power on the sample is estimated to be 7 mW for LCVD-FFF and 20 mW for the remained two. Raman signal was collected with an integration time of 10 s for LCVD-FFF and 4 s for the remained two. The

collected Raman spectra are presented in Fig. 6.2. In the region of carbon bands between 1100 and 1600 cm^{-1}, two peaks at 1350 and 1560 cm^{-1} (Fig. 6.2a-b) are found for Sylramic and Hi-Nicalon S. The former peak is generally assigned to free carbon while the latter corresponds to graphite.[65] This implies a considerable amount of free carbon in the core. The Raman peaks for Si-C bond vibration are generally located in the region between 600 and 1000 cm^{-1}. The transverse optical (TO) phonon band and longitudinal optical (LO) phonon band of 3C-SiC single crystals are expected to present at 796 cm^{-1} and at 972 cm^{-1}, respectively. For Sylramic and Hi-Nicalon S, the two bands are displaced from their nominal position, shifting to lower frequency with increased width due to the nanosized grains. It has been reported that both the peak shift and the peak width are proportional to the inverse of grain size,[66, 67] and also influenced by stacking faults.[68] Therefore, quantitative analysis is not plausible here. Despite this, it can be observed that the two Si-C peaks of Sylramic is sharper and has less shifting than Hi-Nicalon S, agreeing with the observation of l_{XRD}. In the spectrum of LCVD-FFF, only a broad peak can be found in the same region of Raman shift. It is probably due to the small grain size (l_{XRD} = ~7 nm), which heavily disturbs the vibration of Si-C bonds in crystallites.

6.3 Thermal Characterization

SEM images of the samples are shown in Fig. 6.3. As seen, the diameter (30 μm) of the LCVD-based fiber is larger than that (9-11 μm) of the two polymer-precursor-based fibers. The three sampled fibers are straight and uniform in diameter.

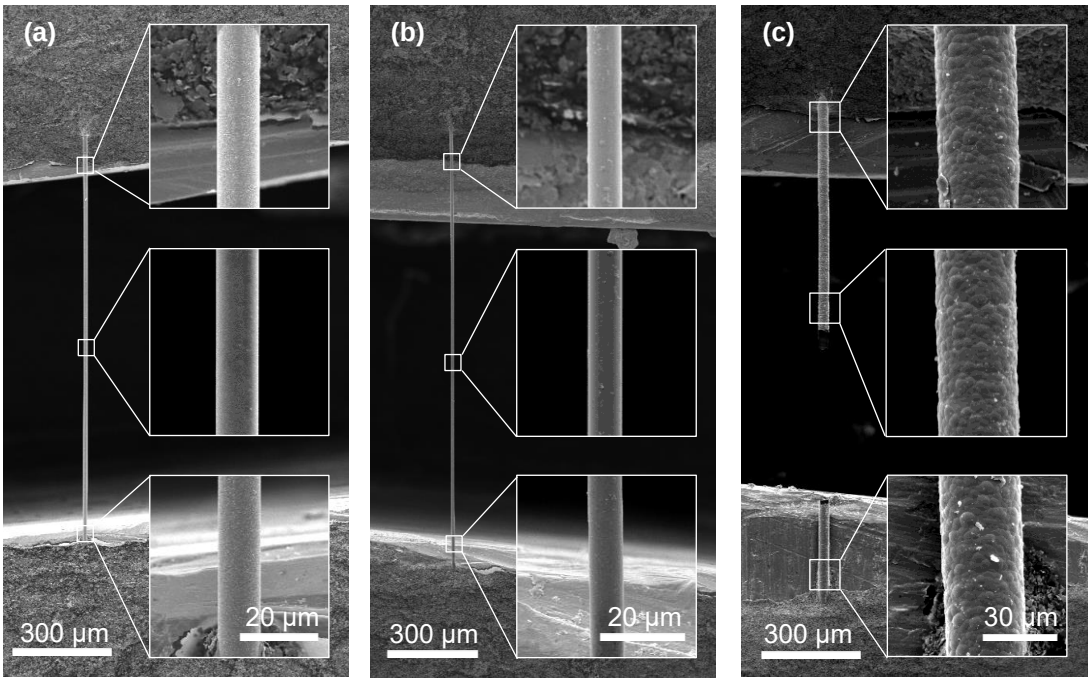

Figure 6.3 SEM images of Sylramic (a), Hi-Nicalon S (b) and LCVD-FFF (c) prepared for TET experiment. For each sample, an overview and three insets are given for showing the length and diameter, respectively. The LCVD-FFF was broken accidentally after thermal characterization.

The temperature dependence of thermal conductivity is presented in Fig. 6.4a. Compared with single crystal and polycrystalline bulk samples of larger grain size from literature,[58, 69] the nanocrystalline microwire samples possess lower thermal conductivities in general and higher characteristic temperatures where thermal conductivity maximizes. The tendency has also been observed for other nanocrystalline structures.[70-73] We attribute the difference in thermal conductivity to the introduction of grain boundaries.

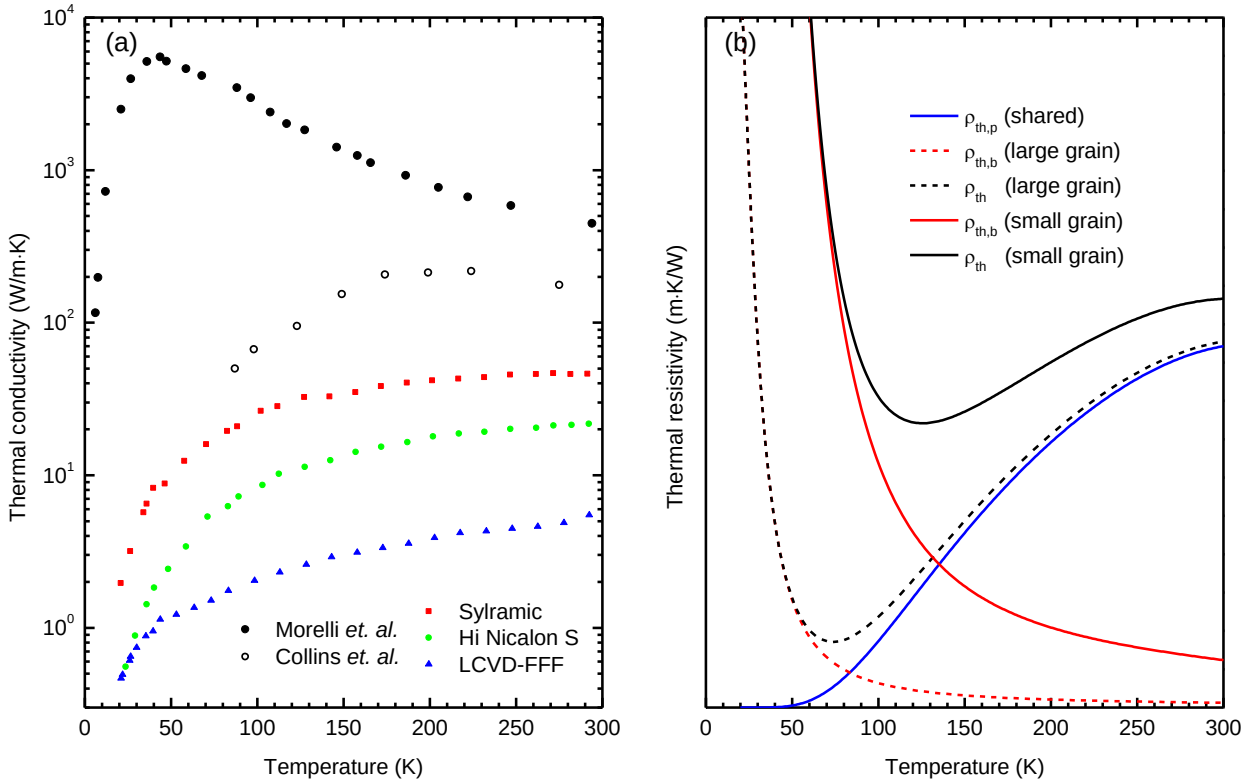

Figure 6.4 (a) Thermal conductivity of Sylramic, Hi-Nicalon S and LCVD-FFF, plotted in semi-log scale. Also shown is the thermal conductivity of SiC single crystal bulk (1-mm grain size) measured by Morelli *et al*.,[69] and SiC polycrystalline bulk (17-μm grain size) by Collins *et al*.[58] (b) Variation of thermal resistivity $\rho_{th,p}$ grain-boundary-induced thermal resistivity $\rho_{th,b}$ and their sum ρ_{th} versus temperature for samples of large grain size and small grain size. $\rho_{th,p}$ is assumed the same for both cases and is therefore denoted as "shared".

The influence of additional grain boundaries (or reduced grain size) on thermal conductivity can be illustrated qualitatively by decomposing the contribution of phonon-phonon scatterings and phonon-boundary scatterings to thermal resistivity $\rho_{th} \equiv k^{-1}$. According to eqn. 1, thermal resistivity can be written as $\rho_{th} = (3/\rho c_p v)(l_b^{-1} + A_0 e^{-T_D/2T})$. Define the fraction induced by phonon-phonon scattering as $\rho_{th,p} = 3A_0 e^{-T_D/2T} / \rho c_p v$, and the fraction induced by phonon-boundary scattering as $\rho_{th,b} = 3/\rho c_p v l_b$. For a given crystal structure with different grain size, $\rho_{th,p}$ is identical while $\rho_{th,b}$ scales with reciprocal of grain size, as depicted in Fig. 6.4b. Due to the

amplified $\rho_{th,b}$, we will see an larger overall ρ_{th} and a shift of minimum ρ_{th} to higher temperature when l_b decreases. Hence, the corresponding thermal conductivity will decrease and maximize at higher temperature as grain size decreases.

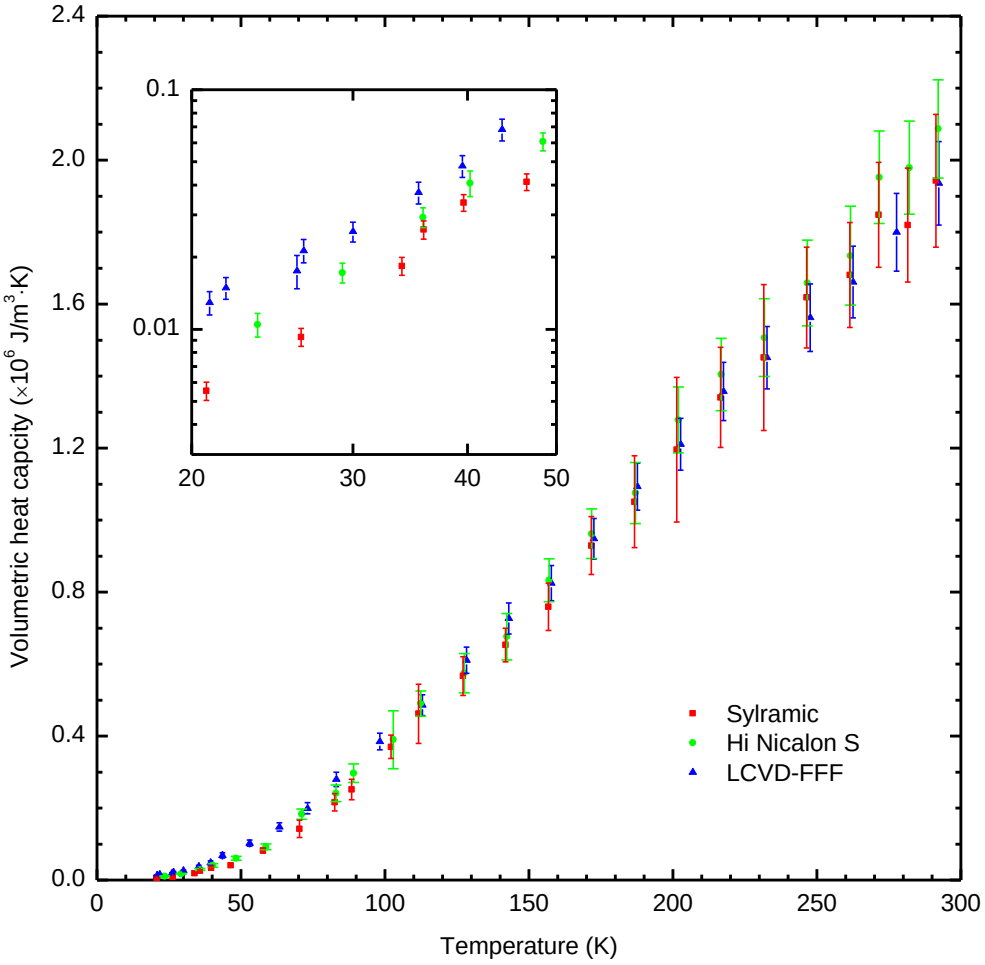

Figure 6.5 Volumetric heat capacity of Sylramic, Hi-Nicalon S and LCVD-FFF. The inset is the volumetric heat capacity between 20 and 50 K, plotted in log-log scale.

Volumetric heat capacity of the samples is shown in Fig. 6.5. Their ρcp is proportional to T as T > 100 K, while the order of temperature dependence is between 2 and 3 as T < 50 K. It is seen that ρc_p of the three samples is not significantly deviates from one another, consistent to Debye's approximation for low-frequency phonons.[74]

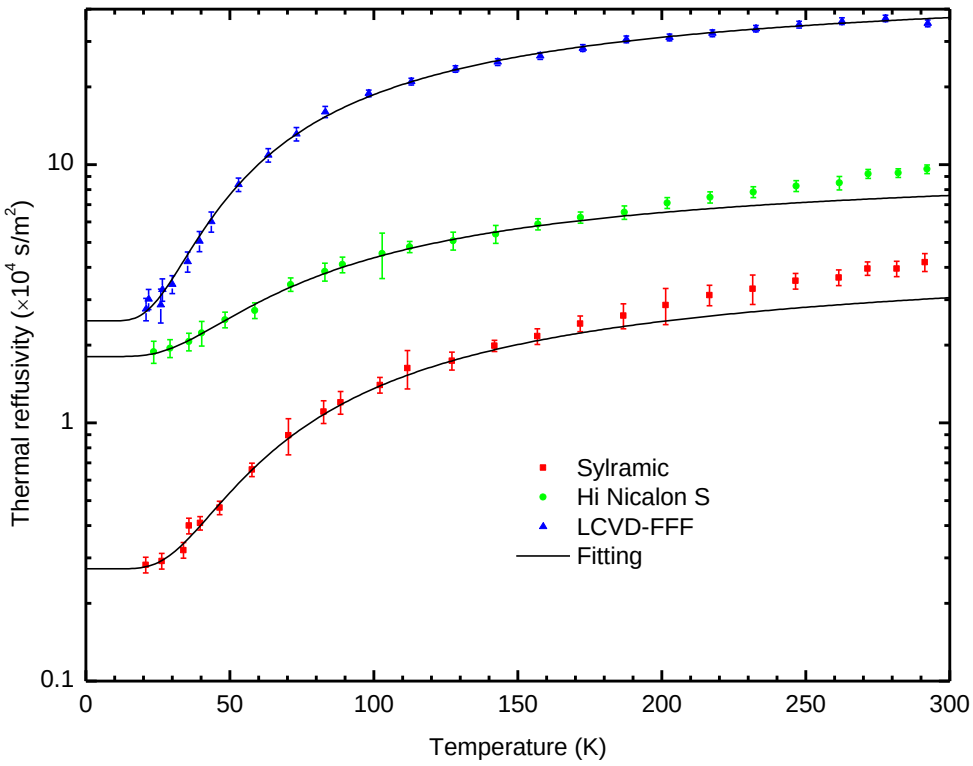

Figure 6.6 Thermal reffusivity of Sylramic, Hi-Nicalon S and LCVD-FFF, plotted in semi-log scale. The fitting function is $\Theta = C\exp(-T_D / 2T) + \Theta_0$, where the constant C, Debye temperature T_D and residual thermal reffusivity Θ_0 are parameters being fitted. In the fitting, Sylramic has Θ_0=2720 m^2/s, C=44503 m^2/s, T_D=282 K; Hi-Nicalon S has Θ_0=18066 m^2/s, C=87283 m^2/s, T_D=246 K; LCVD-FFF has Θ_0=24834 m^2/s, C=506598 m^2/s, T_D=228 K.

The temperature dependence of thermal reffusivity of the three SiC samples is shown in Fig. 6.6. T_D of the three samples is significantly lower than that of 3C-SiC bulk (1000-1300 K) [75] and falls in the range of 220-290 K, suggesting the confinement of high-frequency vibration modes by the nanocrystalline structure. The discrepancy of fitting at high temperature also suggests that some high-frequency modes are allowed for the two samples of larger grain size. The high frequency terms are not added into the formula for the fitting at high temperatures since the discrepancy does not influence the parameters of interest: Θ_0 and STD size. The intercept of the fitting curves Θ_0 is determined to be 2742$\pm$75, 18066$\pm$481 and 24834$\pm$1080 s/m^2, and the

STD size is 9.35±0.56, 1.42±0.08 and 1.03±0.07 nm for Sylramic, Hi-Nicalon S and LCVD-FFF, respectively. The results are summarized in Table 6.1 and compared with the grain size determined by XRD. We find that that STD size is approximately proportional to the grain size. Probably because the STD size and l_{XRD} are related to the scattering effect induced by the same material structure although the former is associated with phonons and the latter is with x-ray photons. In addition, the STD size is about an order of magnitude smaller than l_{XRD}. A possible reason is that the broadening of XRD peak is related to the size of the ordered atoms in a certain direction while the STD size can be confined by the disordered structure in all directions. More specifically, phonon propagation can be constrained by the grain boundaries that do not intersect the propagation path. Therefore, the STD size is smaller than the grain size. Also the much smaller STD size suggests rough grain boundaries that introduces extremely strong phonon scattering. It should be noted that the microstrain[76] and stacking faults[68] that can influence the phonon velocity and phonon lifetime are not taken into account in the modeling of phonon transport here. Despite this, the proportionality between STD size and l_{XRD} provides a very clear correlation between material structure and thermal properties.

Table 6.1 Geometrical parameters and physical data of the three SiC microwire samples.

	L (μm)	D (μm)	k_{RT}* (W/m·K)	Θ_0 (s/cm^2)	l_b (nm)	l_{XRD} (nm)		
						(111)	(220)	(331)
Sylramic	1060	11.1	46.3	0.274	9.35	66.8	113	105
Hi-Nicalon S	1193	9.0	21.7	1.807	1.42	14.6	18.4	15.7
LCVD-FFF	1495	34.3	5.5	2.483	1.03	7.84	7.47	5.85

* k_{RT} denotes the thermal conductivity at room temperature (290 K).

CHAPTER 7. CONCLUSION AND FUTURE WORK

7.1 Conclusion on Human Hair Study

In summary, although the amorphous materials lack long-range order, the short-range order at the atomic length scale still render a domain structure, which reflects the relative structure order level and defect level in the materials. From the above case study, the thermal reffusivity theory successfully evaluates the structural domain size of the human hair of black and grey color. The value of STD size is comparable to the value obtained from the broad peak in XRD. With the help of residual thermal reffusivity value and the STD size, the change of defects levels and domain size in human hair can be obtained. This makes the thermal reffusivity theory a useful tool for studying and comparing the structure of amorphous materials in the future.

7.2 Conclusion on UHMW-PE Microfiber Study

By heat stretching k of UHMWPE microfibers is increased from 19-22 W/m·K to 51.8 W/m·K. It represents the highest repeatable and engineering-level k for PE microfibers. The optimum stretching condition for Spectra S-900 fiber is stretching at 131.5 °C at a strain rate ($0.0129\ s^{-1}$) by a strain ratio of 6.6 followed by quenching in ambient air. Furthermore, we discovered that the amorphous structure fraction increases after stretching, but such more amorphous-composed material rather sustains a much higher k than the highly aligned original sample of higher crystal fraction. A general trend of higher k with higher stretching temperature is observed. k drops when the stretching temperature rises close to the melting point (~146 °C), likely due to the absence of stress when crystallites melt. Calculations based on thermal reffusivity at 0 K limit showed that the structural thermal domain size increases significantly

after heat stretching. XRD pole figure analysis provided evidence that the neither the orientation of nor the size of crystallites were changed by stretching, which points physics reasons to the amorphous region for significant *k* increase. Polarized Raman spectroscopy indicates that the amorphous structure became more aligned after stretching. Aligned amorphous chains lead to enhanced thermal conductivity in amorphous region, which can significantly increase the overall thermal conductivity. The bending test of the stretched samples shows more plasticity, suggesting reduced fraction of amorphous structure among crystallites previously exist in the fiber axial direction. This, even a small amount of reduction in the serially connected amorphous structure, will increase the overall thermal conductivity significantly.

7.3 Conclusion on SiC Microwire Study

We have measured and compared the thermal properties of three advanced SiC microwires in the temperature range of 20-290 K. The room-temperature thermal conductivity of Sylramic, Hi-Nicalon S and LCVD-FFF is 46.3, 21.7 and 5.5 W/m·K, respectively, much smaller than the bulk value. Due to the dominance of phonon-boundary scattering, the Umklapp thermal conductivity ($k \propto T^{-1}$) is not observable in the measured temperature range. The heat capacities obey the classic Debye model. The structural thermal domain size deduced from low-temperature thermal characterization is found to be comparable with the grain size determined by XRD. Specifically, for Sylramic, Hi-Nicalon S and LCVD-FFF, the structural thermal domains were determined as 9.35, 1.42 and 1.03 nm, respectively, proportional to the grain sizes with a factor of 0.1. Hence, a quantitative correlation between grain size and thermal properties is given here for the 3C-SiC microwires.

7.4 Future Work

The study on human hair has shown the potential of applying our thermal characterization technique to examine the structure change in biopolymers. As for biopolymers that feature large molecular weight and lack of long-range order, structure study by XRD and NMR are complicated by the increased linewidths and spectral overlap from large numbers of unique signals. On the contrary, cryogenic thermal characterization by the TET technique can provide an averaged protein domain size without complex configuration and analysis process.

A possible application of this capability is to screen breast cancer. Since 1999, it has been reported that the presence of breast cancer frequently coincides with alternation in hair structure, detected initially by synchrotron XRD[77] and later by Fourier-transform infrared attenuated total reflection (FTIR-ATR).[78] If the altered structure is induced by breast cancer, it is also possible to detect breast cancer with thermal techniques. Besides, the confirmation of the correlation between breast cancer and hair structural alternation still need more large-sample study accounting for different ethnics. In this context, thermal characterization can provide additional evidence for further study and possibly serve as a convenient screening tool in clinical practice. Efforts can be devoted to large-sample study for verifying whether the presence of breast cancer can influence thermal properties of hairs from patients.

Concerning the investigation on UHMW-PE microfibers, it has been shown that polyethylene chains can form a microfiber of metal-like thermal conductivity. It seems, however, difficult to sustain flexibility as thermal conductivity is enhanced, as seen in the bending test for the stretched fiber. In application, the design of soft electronic equipment requires soft electrical insulators. Low-density polyethylene (LD-PE) microfiber may be an excellent candidate for such application if the thermal conductivity can be enhanced via modification of chain alignment. It is

obvious that the maximum thermal conductivity of LD-PE should not be as high as that of UHMW-PE due to the reduced polymer chain length, but LD-PE could be more flexible after being aligned.

In addition, the optimal stretching condition for the UHMW-PE fibers should be further investigated. A noticeable detail during heat stretching is that the section under active deformation may not has a uniform temperature along length, given the heater is merely 5 mm in width and the system is exposed to air. Heat stretching has been a conventional technique for enhancing the thermal conductivity of polymer for decades. Considering the thermal conductivity of the as-stretched fiber is the highest value for polyethylene microfibers to date, it will be highly valuable to investigate if it is the uneven temperature distribution that results in the significantly enhanced thermal conductivity.

REFERENCES

[1] D.G. Cahill, W.K. Ford, K.E. Goodson, G.D. Mahan, A. Majumdar, H.J. Maris, R. Merlin, P. Sr, Nanoscale thermal transport, Journal of Applied Physics, 93 (2003) 793-818.

[2] D.G. Cahill, K. Goodson, A. Majumdar, Thermometry and thermal transport in micro/nanoscale solid-state devices and structures, Journal of Heat Transfer, 124 (2002) 223-241.

[3] W. Yi, L. Lu, D.L. Zhang, Z.W. Pan, S.S. Xie, Linear specific heat of carbon nanotubes, Phys Rev B, 59 (1999) R9015-R9018.

[4] D.G. Cahill, Thermal-Conductivity Measurement from 30-K to 750-K - the 3-Omega Method, Review of Scientific Instruments, 61 (1990) 802-808.

[5] T. Choi, D. Poulikakos, J. Tharian , U. Sennhauser, Measurement of the Thermal Conductivity of Individual Carbon Nanotubes by the Four-Point Three-ω Method, Nano Letters, 6 (2006) 1589-1593.

[6] J. Guo, X. Wang, T. Wang, Thermal characterization of microscale conductive and nonconductive wires using transient electrothermal technique, Journal of Applied Physics, 101 (2007) 063537.

[7] X. Wang, V. Ho, R.A. Segalman, D.G. Cahill, Thermal Conductivity of High-Modulus Polymer Fibers, Macromol., 46 (2013) 4937-4943.

[8] Z. Xu, X. Wang, H. Xie, Promoted electron transport and sustained phonon transport by DNA down to 10 K, Polymer, 55 (2014) 6373-6380.

[9] Y. Xie, Z. Xu, S. Xu, Z. Cheng, N. Hashemi, C. Deng, X. Wang, The Defect Level and Ideal Thermal Conductivity of Graphene Uncovered by Residual Thermal Reffusivity at the 0 K Limit, Nanoscale, 7 (2015) 10101-10110.

[10] Y.S. Xie, P.Y. Yuan, T.Y. Wang, N. Hashemi, X.W. Wang, Switch on the high thermal conductivity of graphene paper, Nanoscale, 8 (2016) 17581-17597.

[11] P.M. Charles Kittel, Introduction to Solid State Physics, 8th ed., John Wiley& Sons, Inc2005.

[12] Characteristics, Applications and Properties of Polymers, in: H.F. Brinson, L.C. Brinson (Eds.) Polymer Engineering Science and Viscoelasticity: An Introduction, Springer US, Boston, MA, 2008, pp. 55-97.

[13] D. Laaber, H.-J. Bart, Chemical Resistance and Mechanical Stability of Polymer Film Heat Exchangers, Chemie Ingenieur Technik, 87 (2015) 306-311.

[14] C.C. Neikirk, J.W. Chung, R.D. Priestley, Modification of mechanical properties in polymer nanocomposites by the incorporation of specific self-complementary hydrogen bonding interactions, Polymer, 79 (2015) 212-220.

[15] L.H. Sperling, Introduction to physical polymer science, John Wiley & Sons2005.

[16] C.L. Choy, Thermal conductivity of polymers, Polymer, 18 (1977) 984-1004.

[17] W.N.D. Santos, R. Gregorio, Hot‐wire parallel technique: A new method for simultaneous determination of thermal properties of polymers, Journal of applied polymer science, 85 (2002) 1779-1786.

[18] B.D. Washo, D. Hansen, Heat Conduction in Linear Amorphous High Polymers: Orientation Anisotropy, Journal of Applied Physics, 40 (1969) 2423-2427.

[19] D.T. Morelli, J. Heremans, M. Sakamoto, C. Uher, Anisotropic Heat Conduction in Diacetylenes, Physical review letters, 57 (1986) 869-872.

[20] L. Piraux, M. Kinany-Alaoui, J.-P. Issi, D. Begin, D. Billaud, Thermal conductivity of an oriented polyacetylene film, Solid state communications, 70 (1989) 427-429.

[21] C. Choy, Y. Wong, G. Yang, T. Kanamoto, Elastic modulus and thermal conductivity of ultradrawn polyethylene, Journal of Polymer Science Part B: Polymer Physics, 37 (1999) 3359-3367.

[22] K. Kurabayashi, Anisotropic Thermal Properties of Solid Polymers, International Journal of Thermophysics, 22 (2001) 277-288.

[23] M.-T. Hung, Heat transport in polymer thin films for micro/nano-manufacturing, ProQuest2007.

[24] J. Liu, R. Yang, Tuning the thermal conductivity of polymers with mechanical strains, Physical Review B, 81 (2010) 174122.

[25] H. Fujishiro, M. Ikebe, T. Kashima, A. Yamanaka, Thermal conductivity and diffusivity of high-strength polymer fibers, Japanese Journal of Applied Physics, 36 (1997) 5633.

[26] J. Ma, Q. Zhang, A. Mayo, Z. Ni, H. Yi, Y. Chen, R. Mu, L.M. Bellan, D. Li, Thermal conductivity of electrospun polyethylene nanofibers, Nanoscale, 7 (2015) 16899-16908.

[27] S. Shen, A. Henry, J. Tong, R. Zheng, G. Chen, Polyethylene nanofibres with very high thermal conductivities, Nat Nano, 5 (2010) 251-255.

[28] A. Henry, G. Chen, High thermal conductivity of single polyethylene chains using molecular dynamics simulations, Physical review letters, 101 (2008) 235-502.

[29] T. Kanamoto, A. Tsuruta, K. Tanaka, M. Takeda, R.S. Porter, Super-drawing of ultrahigh molecular weight polyethylene. 1. Effect of techniques on drawing of single crystal mats, Macromolecules, 21 (1988) 470-477.

[30] C. Choy, W. Leung, Y. Ng, Thermal diffusivity of polymer films by the flash radiometry method, Journal of Polymer Science Part B: Polymer Physics, 25 (1987) 1779-1799.

[31] J. Liu, Z. Xu, Z. Cheng, S. Xu, X. Wang, Thermal Conductivity of Ultrahigh Molecular Weight Polyethylene Crystal: Defect Effect Uncovered by 0 K Limit Phonon Diffusion, ACS Applied Materials & Interfaces, 7 (2015) 27279-27288.

[32] L. Shih, Mesoscopic thermophysical measurements of microstructures and carbon nanotubes, University of California, Berkeley2001.

[33] J.M. Ziman, Electrons and Phonons: the Theory of Transport Phenomena in Solids, Clarendon, Oxford, 1960.

[34] G. Liu, S. Xu, T. Cao, H. Lin, X. Tang, Y. Zhang, X. Wang, Thermally Induced Increase in Energy Transport Capacity of Silkworm Silks, Biopolym., 101 (2014) 1029-1037.

[35] H. Lin, S. Xu, X. Wang, N. Mei, Thermal and Electrical Conduction in Ultrathin Metallic Films: 7 nm down to Sub-Nanometer Thickness, Small, 9 (2013) 2585-2594.

[36] C.H. Deng, Y.M. Sun, L.J. Pan, T.Y. Wang, Y.S. Xie, J. Liu, B.W. Zhu, X.W. Wang, Thermal Diffusivity of a Single Carbon Nanocoil: Uncovering the Correlation with Temperature and Domain Size, Acs Nano, 10 (2016) 9710-9719.

[37] K. Achterhold, C. Keppler, A. Ostermann, U. van Bürck, W. Sturhahn, E.E. Alp, F.G. Parak, Vibrational dynamics of myoglobin determined by the phonon-assisted M\"ossbauer effect, Physical Review E, 65 (2002) 051916.

[38] Murat Kadir, Xinwei Wang, Bowen Zhu, Jing Liu, Duane Harland, C. Popescu, The structure of the ‘‘amorphous” matrix of keratins, Journal of Structural Biology, 198 (2017) 116-123.

[39] C.W. Rudy, A. Marandi, K.L. Vodopyanov, R.L. Byer, In-situ Tapering of Chalcogenide Fiber for Mid-infrared Supercontinuum Generation, (2013) e50518.

[40] A. Henry, G. Chen, High thermal conductivity of single polyethylene chains using molecular dynamics simulations, Physical review letters, 101 (2008) 235502.

[41] S. Chang, Heat-capacities of polyethylene from 2 to 360 K. 2. 2 High-density linear polyethylene samples and thermodynamic properties of crystalline linear polyethylene, Journal of Research of the National Bureau of Standards Section A-Physics and Chemistry, (1974) 387-400.

[42] P. Smith, P.J. Lemstra, J.P.L. Pijpers, A.M. Kiel, Ultra-drawing of high molecular weight polyethylene cast from solution, Colloid and Polymer Science, 259 (1981) 1070-1080.

[43] P. Smith, H.D. Chanzy, B.P. Rotzinger, Drawing of virgin ultrahigh molecular weight polyethylene: An alternative route to high strength/high modulus materials, Journal of Materials Science, 22 (1987) 523-531.

[44] J.-T. Yeh, S.-C. Lin, C.-W. Tu, K.-H. Hsie, F.-C. Chang, Investigation of the drawing mechanism of UHMWPE fibers, Journal of Materials Science, 43 (2008) 4892-4900.

[45] C.L. Choy, W.H. Luk, F.C. Chen, Thermal conductivity of highly oriented polyethylene, Polymer, 19 (1978) 155-162.

[46] Y.L. Hsieh, X.P. Hu, Structural transformation of ultra‐high modulus and molecular weight polyethylene fibers by high‐temperature wide‐angle X‐ray diffraction, Journal of Polymer Science Part B: Polymer Physics, 35 (1997) 623-630.

[47] C. Fagnano, M. Rossi, R.S. Porter, S. Ottani, A study on solid-state drawn fibers of polyethylene by confocal Raman microspectrometry: evaluation of the orientation profiles of amorphous and crystalline phases across the fiber section, Polymer, 42 (2001) 5871-5883.

[48] S. Kavesh, D.C. Prevorsek, Ultra High Strength, High Modulus Polyethylene Spectra Fibers and Composites, International Journal of Polymeric Materials and Polymeric Biomaterials, 30 (1995) 15-56.

[49] G. Kalaprasad, P. Pradeep, G. Mathew, C. Pavithran, S. Thomas, Thermal conductivity and thermal diffusivity analyses of low-density polyethylene composites reinforced with sisal, glass and intimately mixed sisal/glass fibres, Composites Science and Technology, 60 (2000) 2967-2977.

[50] Stein, Norris, The x-ray diffraction, birefringence, and infrared dichroism of stretched polyethylene, J. Poly. Sci., 21 (1956) 381-396.

[51] D.R. Holmes, R.P. Palmer, The orientation of the crystalline and amorphous regions in polyethylene film, Journal of Polymer Science, 31 (1958) 345-358.

[52] Y. Takahashi, L. Puppulin, W. Zhu, G. Pezzotti, Raman tensor analysis of ultra-high molecular weight polyethylene and its application to study retrieved hip joint components, Acta Biomaterialia, 6 (2010) 3583-3594.

[53] H.M. Yun, J.A. DiCarlo, Comparison of the Tensile, Creep, and Rupture Strength Properties of Stoichiometric SiC Fibers, Ceram. Eng. Sci. Proc., 20 (1999) 259-272.

[54] M. Takeda, J. Sakamoto, A. Saeki, Y. Imai, H. Ichikawa, High-performance Silicon Carbide Fiber Hi-Nicalon for Ceramic Matrix Composites, Ceram. Eng. Sci. Proc., 16 (1995) 37-44.

[55] A.R. Bunsell, M.H. Berger, Fine Diameter Ceramic Fibres, J. Eur. Ceram. Soc., 20 (2000) 2249-2260.

[56] S. Dong, G. Chollon, C. Labrugere, M. Lahaye, A. Guette, J. Bruneel, M. Couzi, R. Naslain, D. Jiang, Characterization of Nearly Stoichiometric SiC Ceramic Fibres, J. Mater. Sci., 36 (2001) 2371-2381.

[57] J.A. DiCarlo, H.-M. Yun, Non-oxide (Silicon Carbide) Fibers, in: N.P. Bansal (Ed.) Handbook of Ceramic Composites, Springer US, Boston, MA, 2005, pp. 33-52.

[58] A.K. Collins, M.A. Pickering, R.L. Taylor, Grain Size Dependence of the Thermal Conductivity of Polycrystalline Chemical Vapor Deposited β-SiC at Low Temperatures, J. Appl. Phys., 68 (1990) 6510-6512.

[59] K. Minato, K. Fukuda, Structure of Chemically Vapour Deposited Silicon Carbide for Coated Fuel Particles, J. Mater. Sci., 23 (1988) 699-706.

[60] H. Kaifu, H. Yemin, M. Yanwen, L. Yinong, H. Zheng, C. Yi, Synthesis and field emission properties of titanium carbide nanowires, Nanotechnol., 18 (2007) 145615.

[61] K. Koumoto, S. Takeda, C.H. Pai, T. Sato, H. Yanagida, High-Resolution Electron Microscopy Observations of Stacking Faults in β-SiC, J. Am. Ceram. Soc., 72 (1989) 1985-1987.

[62] F. Solá, R. Bhatt, Mapping the Local Modulus of Sylramic Silicon Carbide Fibers by Nanoindentation, Mater. Lett., 159 (2015) 395-398.

[63] P.J. Baxter, C. Bonadonna, R. Dupree, V.L. Hards, S.C. Kohn, M.D. Murphy, A. Nichols, R.A. Nicholson, G. Norton, A. Searl, R.S.J. Sparks, B.P. Vickers, Cristobalite in Volcanic Ash of the Soufriere Hills Volcano, Montserrat, British West Indies, Science, 283 (1999) 1142-1145.

[64] C. Elmi, J. Chen, D. Goldsby, R. Gieré, Mineralogical and compositional features of rock fulgurites: A record of lightning effects on granite, Am. Mineral., 102 (2017) 1470.

[65] G. Chollon, R. Pailler, R. Naslain, F. Laanani, M. Monthioux, P. Olry, Thermal Stability of a PCS-derived SiC Fibre with a Low Oxygen Content (Hi-Nicalon), J. Mater. Sci., 32 (1997) 327-347.

[66] G. Gouadec, P. Colomban, Raman Spectroscopy of Nanomaterials: How Spectra Relate to Disorder, Particle Size and Mechanical Properties, Prog. Cryst. Growth Character. Mater., 53 (2007) 1-56.

[67] R. Nemanich, S. Solin, R.M. Martin, Light scattering study of boron nitride microcrystals, Phys. Rev. B, 23 (1981) 6348.

[68] J. Lipowitz, J.A. Rabe, A. Zangvil, Y. Xu, Structure and properties of Sylramic silicon carbide fiber—a polycrystalline, stoichiometric β-SiC composition, Ceram. Eng. Sci. Proc., 18 (1997) 147-157.

[69] D.T. Morelli, J.P. Heremans, G.A. Slack, Estimation of the Isotope Effect on the Lattice Thermal Conductivity of Group IV and Group III-V Semiconductors, Phys. Rev. B, 66 (2002) 195304.

[70] D. Li, Y. Wu, P. Kim, L. Shi, P. Yang, A. Majumdar, Thermal Conductivity of Individual Silicon Nanowires, Appl. Phys. Lett., 83 (2003) 2934-2936.

[71] N. Mingo, L. Yang, D. Li, A. Majumdar, Predicting the Thermal Conductivity of Si and Ge Nanowires, Nano Letters, 3 (2003) 1713-1716.

[72] R. Chen, A.I. Hochbaum, P. Murphy, J. Moore, P. Yang, A. Majumdar, Thermal Conductance of Thin Silicon Nanowires, Phys. Rev. Lett., 101 (2008) 105501.

[73] Z. Wang, J.E. Alaniz, W. Jang, J.E. Garay, C. Dames, Thermal conductivity of nanocrystalline silicon: importance of grain size and frequency-dependent mean free paths, Nano letters, 11 (2011) 2206-2213.

[74] C. Kittel, Introduction to Solid State Physics, 8th ed., John Wiley & Sons New York, United States, 2005.

[75] O. Madelung, U. Rössler, M. Schulz, Semiconductors: Group IV Elements, IV–IV and III–IV compounds, Landolt-Börnstein, New series, Group III, vol. 41, part A, Springer-Verlag, Berlin, 2005.

[76] M. Fujii, Y. Kanzawa, S. Hayashi, K. Yamamoto, Raman Scattering from Acoustic Phonons Confined in Si Nanocrystals, Phys. Rev. B, 54 (1996) R8373.

[77] V. James, J. Kearsley, T. Irving, Y. Amemiya, D. Cookson, Using hair to screen for breast cancer, Nature, 398 (1999) 33.

[78] D.J. Lyman, J. Murray-Wijelath, Fourier transform infrared attenuated total reflection analysis of human hair: comparison of hair from breast cancer patients with hair from healthy subjects, Applied spectroscopy, 59 (2005) 26-32.